

**A Computational Assessment of Laminar Flame Speed Correlation in  
an Ultralean Prechamber Engine**

Thesis by

Ghufran Alkhamis

In Partial Fulfillment of the Requirements

For the Degree of

Master of Science

King Abdullah University of Science and Technology

Thuwal, Kingdom of Saudi Arabia

November, 2021

**EXAMINATION COMMITTEE PAGE**

The thesis of Ghufuran Alkhamis is approved by the examination committee.

Committee Chairperson: Prof. Hong G. Im

Committee Members: Prof. James W. Turner, Prof. Shuyu Sun

© November, 2021

Ghufran Alkhamis

All Rights Reserved

## ABSTRACT

### A Computational Assessment of Laminar Flame Speed Correlation in an Ultralean Prechamber Engine

Ghufran Alkhamis

Predictive modeling of pre-chamber combustion engines relies primarily on the correct prediction of laminar and turbulent flame speeds. While the latter has been rigorously derived, the former correlations are mostly semi-empirical and valid for a limited range of operating conditions. The current work aims at highlighting the fundamental significance of correct laminar flame speed prediction on numerical modeling of ultralean prechamber engine combustion. Gulder's empirical correlation for laminar flame speed was chosen for the current work. It was modified for ranges beyond what it was originally derived for. It was initially observed that the numerical results that utilize Gulder's correlation for the laminar flame speed underperform compared to the one computed from the skeletal GRI3.0 by Lu and Law. In all cases, Peters' turbulent flame speed correlation was used, which evidences that any potential difference comes from the laminar flame speed. Using Lu and Law's chemical mechanism as a reference for laminar flame speed calculations, the values of the empirical constants  $\alpha$ ,  $\eta$ , and  $\xi$  in Gulder's correlation were optimized to yield more accurate flame speeds at ultralean engine conditions. The updated Gulder's correlation for methane was implemented in CONVERGE, a three-dimensional computational fluid

dynamics (CFD) solver, and validated against the experimental engine results from KAUST. The flame topology was also explored to correlate the observed behaviors in the pressure predictions among all tested cases. Finally, the Borghi-Peters diagram provides insightful information on combustion regimes encountered in pre-chamber combustion engines.

## ACKNOWLEDGEMENTS

I would like to thank my advisor and committee chair, Prof. Hong G. Im, for the opportunity to join the Computational Reaction Flow Laboratory (CRFL) within the Clean Combustion Research Center (CCR) at KAUST. I would like to extend my thanks to my senior PhD student, Mickael Silva, for his guidance and support throughout technical aspects of the work. I want to thank the committee members for their valuable feedback on the editorial and scientific aspects of this work. Lastly, my thanks to the KAUST experimental team led by Professor James Turner, who kindly provided experimental data for the initial validation of the current work.

My deepest gratitude and appreciation go to my community of friends at King Abdullah University for Science and Technology for making my experience exceptional and fulfilling.

## TABLE OF CONTENTS

<b>EXAMINATION COMMITTEE PAGE .....</b>	<b>2</b>
<b>COPYRIGHT PAGE.....</b>	<b>3</b>
<b>ABSTRACT.....</b>	<b>4</b>
<b>ACKNOWLEDGEMENTS .....</b>	<b>6</b>
<b>TABLE OF CONTENTS .....</b>	<b>7</b>
<b>LIST OF ABBREVIATIONS .....</b>	<b>9</b>
<b>LIST OF SYMBOLS .....</b>	<b>10</b>
<b>LIST OF ILLUSTRATIONS.....</b>	<b>11</b>
<b>Chapter 1 .....</b>	<b>13</b>
<b>Introduction.....</b>	<b>13</b>
<b>Chapter 2 .....</b>	<b>17</b>
<b>Flame Speed Model and Correlations.....</b>	<b>17</b>
2.1 <i>G</i> -Equation .....	17
2.2 Turbulence Modeling .....	18
2.3 Laminar Flame Speed.....	21
2.4 Turbulent Flame Speed .....	22
<b>Chapter 3 .....</b>	<b>25</b>
<b>Numerical Setup.....</b>	<b>25</b>
3.1 1-D Model Setup .....	25
3.2 CONVERGE setup.....	27
<b>Chapter 4 .....</b>	<b>29</b>
<b>Optimization and 1-D Flame Speed Assessment.....</b>	<b>29</b>
4.1 Gulder’s Model Constants.....	29
4.2 Constants Optimization Method.....	32
4.2 1-D Laminar Flame Assessment .....	34
4.2 Summary .....	36
<b>Chapter 5 .....</b>	<b>37</b>

<b>3D CFD Results</b> .....	<b>37</b>
5.1 Effect of Updated Laminar Burning Velocity.....	37
5.2 Analysis of Damköhler Number and Borghi-Peters Diagram in Pre and Main Chambers.....	43
5.4 Summary .....	60
<b>Chapter 6</b> .....	<b>62</b>
<b>Conclusion and Future Work</b> .....	<b>62</b>
<b>BIBLIOGRAPHY</b> .....	<b>65</b>

**LIST OF ABBREVIATIONS**

<b>AMR</b>	adaptive mesh refinement
<b>ATDC</b>	after top dead center
<b>CAD</b>	crank angle degree
<b>CFD</b>	computational fluid dynamics
<b>DNS</b>	direct numerical simulations
<b>RANS</b>	Reynolds-averaged Navier-Stokes
<b>RNG</b>	Renormalization Group
<b>PCFR</b>	Prechamber fueling ratio

**LIST OF SYMBOLS**

$\lambda$	Air-fuel ratio
$\phi$	Fuel-air ratio
$\alpha$	Temperature exponent in Gulder's correlation for laminar flame speed
$\beta$	Pressure Exponent in Gulder's correlation for laminar flame speed
$\eta$	Empirical constant in Gulder's correlation for laminar flame speed
$\xi$	Empirical constant in Gulder's correlation for laminar flame speed
$S_L$	Laminar flame speed
$S_T$	Turbulent flame speed

## LIST OF ILLUSTRATIONS

Figure 1: Chemkin setup validation for the reduced GRI mechanism.....	26
Figure 2: $S_L$ as determined by various chemical mechanisms at ambient conditions. ....	27
Figure 3: Variation in Gulder’s $S_L$ within the Gulder’s range of $\alpha$ at high pressure and temperature .....	31
Figure 4: Percent difference between the two $S_L$ for the range of $\alpha = 1 - 4$ .....	33
Figure 5: $S_L$ - Gulder vs. skeletal GRI – for a wide temperature range and $P=40\text{atm}$ .....	34
Figure 6: $S_L$ – updated Gulder vs. skeletal GRI - for wide temperature range and $P=40\text{atm}$ .....	35
Figure 7: CFD and 3D results for tabulated mechanism and Gulder’s original and updated models with PCFR 3% .....	38
Figure 8: CFD and 3D results for tabulated mechanism and Gulder’s original and updated models with PCFR 7% .....	41
Figure 9: CFD and 3D results for tabulated mechanism and Gulder’s original and updated models with PCFR 13% .....	42
Figure 10: 3D results of the prechamber composition at spark time (-13 CAD).....	43
Figure 11: Prechamber pressure as predicted by the reference case, Gulder’s original model, and Gulder’s updated model for the case of PCFR 3% .....	44
Figure 12: 3D results of flame topology and Damköhler number within the prechamber region for the three models for the case of PCFR 3% .....	45
Figure 13: Main chamber pressure predicted by the reference case, Gulder’s original model, and Gulder’s updated model for the case of PCFR 3% .....	46
Figure 14: 3D results of flame topology and Damköhler number within the main chamber region for the three models for the case of PCFR 3% .....	47
Figure 15: Borghi-Peters diagram for PCFR 3% showing the base case and Gulder’s original model .....	48
Figure 16: Borghi-Peters diagram for PCFR 3% showing the base case and Gulder’s updated model .....	49

Figure 17: Prechamber pressure as predicted by the reference case, Gulder's original model, and Gulder's updated model for the case of PCFR 7% .....	50
Figure 18: 3D results of flame topology and Damköhler number within the prechamber region for the three models for the case of PCFR 7% .....	51
Figure 19: Main chamber pressure as predicted by the reference case, Gulder's original model, and Gulder's updated model for the case of PCFR 7% .....	52
Figure 20: 3D results of flame topology and Damköhler number within the main chamber region for the three models for the case of PCFR 7% .....	53
Figure 21: Borghi-Peters diagram for PCFR 7% showing the base case and Gulder's original model .....	54
Figure 22: Borghi-Peters diagram for PCFR 7% showing the base case and Gulder's updated model .....	55
Figure 23: Prechamber pressure as predicted by the reference case, Gulder's original model, and Gulder's updated model for the case of PCFR 13% .....	56
Figure 24: 3D results of flame topology and Damköhler number within the prechamber region for the three models for the case of PCFR 13% .....	57
Figure 25: Main chamber pressure as predicted by the reference case, Gulder's original model, and Gulder's updated model for the case of PCFR 13% .....	58
Figure 26: 3D results of flame topology and Damköhler number within the main chamber region for the three models for the case of PCFR 13% .....	58
Figure 27: Borghi-Peters diagram for PCFR 13% showing the base case and Gulder's original model .....	59
Figure 28: Borghi-Peters diagram for PCFR 13% showing the base case and Gulder's updated model .....	60

## Chapter 1

### Introduction

A major driving force in the field of internal combustion engines research is the necessity for lower emissions and high fuel efficiency while maintaining a reasonable cost. The option of lean-burn condition can directly solve the proposed issues by decreasing the NO<sub>x</sub> emissions below the standard emissions level and reducing the fuel consumption [1]. However, exceeding the flammability limit makes engine operation under lean conditions with a conventional spark plug more difficult [2]. The prechamber engine was, hence, designed to extend flammability limits of SI engines operation. Instead of being ignited by a spark plug alone, the homogenous and ultra-lean charge in the main chamber is ignited by highly turbulent and reactive jets issued from the prechamber.

The charge in the relatively small-sized prechamber is ignited using a spark plug. The flame propagates from the prechamber into the main chamber through the connecting nozzles. The combustion of the lean mixture in the main chamber is then initiated by the jets issued from the prechamber. The jets have high temperatures, are highly turbulent, and contain highly reactive radicals. Multiple works have attempted to investigate the effect of the prechamber composition [3], the prechamber geometry [4-6], and spark plug location on the main chamber combustion [7].

Due to the nature of the operating conditions encountered in prechamber combustion engines, the accuracy of numerical modeling of such devices is still an evolving mission. The recent predictive modeling of the prechamber and main chamber

pressure and heat release rate is found to be inconsistent with the obtained experimental engine data [2, 8]. To resolve this issue, several works [2, 8] adjusted the turbulence-related model constants in Peters' turbulent flame speed correlation, aiming to match the numerical results with the experimental data without a consistent rationale. Those constants were derived through rigorous mathematics, as shown in Peters' work. Since the values of those constants were not selected initially to fit his empirical expression into the experimental data, additional modifying of the values would not be an appropriate approach [9]. In fact, this method of adjusting Peters' model constants is case specific and, hence, does not yield a general solution to the posed issue of numerical model accuracy.

The laminar flame speed is a crucial component of combustion prediction that has not been investigated in relation to the accuracy of numerical modeling. Indeed, the turbulent flame speed ( $S_T$ ), as calculated by Peters' correlation, is a magnification of the laminar flame speed ( $S_L$ ) caused by flame front corrugation due to turbulence [10]. Therefore, if  $S_L$  is inaccurate,  $S_T$  will be inherently imprecise. Commonly known semi-empirical flame speed correlations, like Gulder's, are curve fit and are obtained for multiple fuels within a limited range of pressure and temperature. This results in no guarantee that these correlations are valid at ultralean engine conditions. Consequently, adjusting the laminar flame speed correlations can be a consistent route towards improving the predictive modeling of prechamber combustion engines.

The laminar flame speed correlations are functions of temperature, pressure, and equivalence ratio. Nearly all suggested correlations for the laminar flame speed agree on exponential dependence of  $S_L$  on both temperature and pressure [11]. The value of the

pressure dependence coefficient is similar in most of the known correlations for  $S_L$ . At ambient and near ambient temperature and pressure conditions, the value of the temperature dependence coefficient is mainly agreed upon to be around 2. At high temperature and pressure conditions, the value of the temperature constant greatly differs in literature due to the limited experimental data available at such conditions [11].

Gulder's correlation [11] is one of the most commonly used relations for calculating  $S_L$  and is already implemented in the CFD solver CONVERGE. Therefore, it is investigated in this work and is selected to assess the effect of  $S_L$  on the predictive modeling of prechamber engine combustion. In his correlation, similar to most other correlations,  $S_L$  is a function of the ratio of the unburned temperature to the ambient temperature  $S_L \propto \left(\frac{T_{unburned}}{T_{ambient}}\right)^\alpha$ . For methane, he states that  $\alpha$  has a value between 1.37 and 2.33 depending on the pressure and equivalence ratio used. Andrews and Bradley [12], in their investigation on the burning velocity of methane-air mixtures, suggest that  $\alpha = 2$  and its value indeed differs based on the pressure and equivalence ratio. Babkin and Kozachenko [13] show in their extensive study on the effect of high pressure on the normal burning velocity of methane that the value of  $\alpha \geq 2$  for the range of pressure of 1-70 [atm]. Therefore, the exact value of the temperature exponent ( $\alpha$ ) remains a debate and depends highly on the operating conditions. This work will, hence, attempt to optimize the value of  $\alpha$  for the selected engine conditions.

Furthermore, some of the chemical mechanisms available to calculate the laminar flame speed are the detailed GRI 3.0 [14], reduced GRI 3.0 by Lu and Law [15], Aramco [16], and UCSD [17]. At ambient conditions, all the mentioned mechanisms calculate

similar values for  $S_L$  as a function of equivalence ratio. Previous CFD works [3, 5, 7, 18] utilized the skeletal GRI 3.0 by Lu and Law and obtained satisfactory prediction of ultra-learn prechamber experimental engine data. Therefore, the skeletal GRI mechanism was selected as a reference case for the 1-D calculation of the laminar flame speed. While Gulder's correlation and the skeletal GRI mechanism calculate similar laminar burning velocity at ambient temperature and pressure, they disagree widely at the high engine conditions encountered in prechamber combustion.

The primary objective of this study is to demonstrate the effect of the laminar flame speed on the prediction of the turbulent flame speed in numerical modeling of prechamber engine combustion. Using the calculations of  $S_L$  by the skeletal GRI mechanism as a baseline, the empirical constants in Gulder's  $S_L$  correlation will be adjusted to reflect the specific prechamber engine operating conditions. The optimized Gulder's relation is then implemented in CONVERGE to assess its ability to predict the KAUST prechamber experimental engine results.

## Chapter 2

### Flame Speed Model and Correlations

#### 2.1 G-Equation

The level set approach based on the  $G$ -equation is used for the modeling of premixed turbulent combustion. The non-reacting scalar  $G$  is derived from the iso-scalar surface  $G(\mathbf{x}, t)$  which denotes the mean flame front position (at  $G = 0$ ) and divides the flow into the unburnt mixture region ( $G < 0.0$ ), and the burnt gas region ( $G > 0.0$ ). Beyond the flame surface,  $\left| \frac{\partial G}{\partial x_i} \right| = 1$ . Therefore, the  $G$ -equation is a scalar three-dimensional field equation used to describe the instantaneous flame front position. It has properties similar to other field equations used in fluid dynamics [9]. The equation was originally derived by Forman Williams [19] for the corrugated flamelet regime and later adjusted to be valid for the thin reaction zone regime as well. Therefore, the  $G$ -equation is only valid when the flame is in the thin reaction zone or the corrugated flamelet regime [9]. The field equation determines the flame front position by solving for the mean of  $G$  in the following equation:

$$\frac{\partial \rho \tilde{G}}{\partial t} + \frac{\partial \rho \tilde{u}_i \tilde{G}}{\partial x_i} = -\rho D'_t \tilde{\kappa} \left| \frac{\partial \tilde{G}}{\partial x_i} \right| + \rho_u s_t \left| \frac{\partial \tilde{G}}{\partial x_i} \right| \quad (2.1)$$

where  $\rho_u$  is the density of the unburnt mixture,  $s_t$  is the turbulent flame speed,  $c_s$  is a used-supplied constant,  $\varepsilon$  is the turbulent dissipation, and  $k$  is the turbulent kinetic energy.  $D'_t$

denotes the turbulent diffusion terms and, when the variance of  $G$  is not solved, are calculated as:

$$D'_t = \frac{c_\mu k^2}{Sc \varepsilon} \quad (2.2)$$

The mean flame curvature is given by:

$$\tilde{\kappa} = - \frac{\partial}{\partial x_i} \left( \frac{\partial \tilde{G}}{\partial x_i} / \left| \frac{\partial \tilde{G}}{\partial x_i} \right| \right) \quad (2.3)$$

## 2.2 Turbulence Modeling

The Reynolds-Average Navier-Stokes (RANS) turbulence model decomposes the flow velocity into an ensemble mean term and a fluctuating term

$$u_i = \bar{u}_i + u'_i \quad (2.4)$$

Substituting the velocity decomposition equation into the Navier-Stokes equations yields the RANS equations for mass and momentum transport.

$$\frac{\partial \bar{\rho}}{\partial t} + \frac{\partial \bar{\rho} \tilde{u}_j}{\partial x_j} = 0 \quad (2.5)$$

$$\begin{aligned}
& \frac{\partial \bar{\rho} \tilde{u}_i}{\partial t} + \frac{\partial \bar{\rho} \tilde{u}_i \tilde{u}_j}{\partial x_j} \\
& = -\frac{\partial \bar{P}}{\partial x_i} + \frac{\partial}{\partial x_j} \left[ \mu \left( \frac{\partial \tilde{u}_i}{\partial x_j} + \frac{\partial \tilde{u}_j}{\partial x_i} \right) - \frac{2}{3} \mu \left( \frac{\partial \tilde{u}_k}{\partial x_k} \delta_{ij} \right) \right] \\
& + \frac{\partial}{\partial x_j} (-\bar{\rho} \tilde{u}'_i \tilde{u}'_j)
\end{aligned} \tag{2.6}$$

The last term in the momentum equation refers to Reynolds stress term and represents the effects of turbulence and is introduced by the ensemble averaging of the equations, which need to be closed or modeled.

### 2.2.1 The RNG $k - \varepsilon$ Model

To model the Reynolds stress term in the RANS equations, two additional equations are used in the RNG (Renormalization Group)  $k - \varepsilon$  model. One equation is for  $k$ , the turbulent kinetic energy, and the other is for  $\varepsilon$ , the dissipation of the turbulent kinetic energy. The Reynold stress is modeled as:

$$\tau_{ij} = -\bar{\rho} \tilde{u}'_i \tilde{u}'_j = 2\mu_t S_{ij} - \frac{2}{3} \delta_{ij} \left( \rho k + \mu_t \frac{\partial \tilde{u}_i}{\partial x_i} \right) \tag{2.7}$$

The turbulent viscosity and the turbulent kinetic energy are defined as:

$$\mu_t = C_\mu \rho \frac{k^2}{\varepsilon} , \quad k = \frac{1}{2} \tilde{u}'_i \tilde{u}'_i \tag{2.8}$$

where  $C_\mu = 0.09$  is a model constant. The mean stress rate tensor is:

$$S_{ij} = \frac{1}{2} \left( \frac{\partial \tilde{u}_i}{\partial x_j} + \frac{\partial \tilde{u}_j}{\partial x_i} \right) \quad (2.9)$$

The turbulent diffusion ( $D_t$ ) and conductivity ( $K_t$ ) are computed as

$$D_t = \frac{\mu_t}{\rho S c_t} \quad (2.10)$$

$$K_t = \frac{\mu_t}{\rho Pr_t} C_p \quad (2.11)$$

where  $Sc_t$  and  $Pr_t$  are the turbulent Schmidt number and the turbulent Prandtl number, respectively. The two equations for the turbulent kinetic energy and the dissipation of the turbulent kinetic energy are:

$$\frac{\partial \rho k}{\partial t} + \frac{\partial \rho u_i k}{\partial x_i} = \tau_{ij} \frac{\partial u_i}{\partial x_j} + \frac{\partial}{\partial x_j} \frac{\mu + \mu_t}{Pr_k} \frac{\partial k}{\partial x_j} - \rho \varepsilon + \frac{C_s}{1.5} S_s \quad (2.12)$$

$$\frac{\partial \rho \varepsilon}{\partial t} + \frac{\partial (\rho u_i \varepsilon)}{\partial x_i} = \frac{\partial}{\partial x_j} \left( \frac{\mu + \mu_t}{Pr_\varepsilon} \frac{\partial \varepsilon}{\partial x_j} \right) + C_{\varepsilon 3} \rho \varepsilon \frac{\partial u_i}{\partial x_i} + \frac{\varepsilon}{k} \left( C_{\varepsilon 1} \frac{\partial u_i}{\partial x_j} \tau_{ij} - C_{\varepsilon 2} \rho \varepsilon C_s S_s \right) + S - \rho R_\varepsilon \quad (2.13)$$

where the 1.5 is an empirical constant,  $S$  is a user-defined source term,  $S_s$  the source term that includes interactions with discrete phase ( $=0$  in the case of gaseous flows), and  $C_{\varepsilon i}$  terms are model constants that represent compression and expansion. Finally,

$$R_\varepsilon = \frac{C_\mu \eta^3 (1 - \eta / \eta_0) \varepsilon^2}{(1 + \beta \eta^3) k} \quad (2.14)$$

$$\eta = \frac{k}{\varepsilon} |S_{ij}| = \frac{k}{\varepsilon} \sqrt{2 S_{ij} S_{ij}} \quad (2.15)$$

## 2.3 Laminar Flame Speed

The normal velocity of the flame front propagation, relative to the flow in the direction of the unburnt mixture, is called the laminar flame speed ( $S_L$ ). It is a transport property and a function of the unburnt mixture temperature, pressure, and equivalence ratio [9]. The laminar flame speed can be measured experimentally or numerically using extensive or reduced chemical mechanisms.

$S_L$  for the methane-air mixture can also be calculated using one of the available empirical or semi-empirical correlations [11]. The most commonly used correlation is the empirical expression suggested by Gulder [11]:

$$S_u(\phi, T, P) = S_{u0}(\phi) \left[ \frac{P_u}{P_o} \right]^\beta \left[ \frac{T_u}{T_o} \right]^\alpha \quad (2.16)$$

where

$$S_{u0}(\phi) = z W \phi^\eta \exp[-\xi(\phi - 1.075)^2] \quad (2.17)$$

$S_{u0}$  is the room temperature burning velocity,  $P_o = 1 \text{ atm}$ ,  $T_o = 300 \text{ K}$ ,  $\alpha = 1.37 - 2.33$ ,  $\beta = -0.5$ ,  $Z = 1$ ,  $W [m/s] = 0.422$ ,  $\eta = 0.15$ , and  $\xi = 5.18$  for methane as stated by Gulder (1984) [11].

Gulder measured the methane-air burning velocities experimentally in a constant-volume spherical bomb with a diameter of 0.325 m with a density correction scheme [11]. The empirical correlation in (2.17) was then selected to represent the normal burning velocity at ambient temperature and pressure. The temperature and pressure dependence

coefficients were then determined separately by examining the variation in  $S_u$  with  $\frac{T_u}{T_o}$  and  $\frac{P_u}{P_o}$ , respectively.

Therefore, according to Gulder, the values of  $\eta$ , and  $\xi$  are fuel-dependent and were determined empirically to curve fit the expression in (2.17) into the experimental data for  $S_L$  of methane at room temperature (300 K) [11]. The range of values for  $\alpha$  was then selected to scale the expression of  $S_L$  into the experimental measurements of the burning velocity conducted at higher temperatures (>300 K).

## 2.4 Turbulent Flame Speed

The premixed turbulent flame speed ( $S_T$ ) depends on local mean quantities. It is the speed at which the mean turbulent flame front propagates relative to the flow field. The full derivation of the turbulent burning velocity [9] is not shown here. The correlation used for the turbulent velocity is that provided by Peters [9]:

$$S_T = S_L + u' \left\{ -\frac{a_4 b_3^2}{2b_1} Da + \left[ \left( \frac{a_4 b_3^2}{2b_1} Da \right)^2 + a_4 b_3^2 Da \right]^{1/2} \right\} \quad (2.18)$$

where  $u'$  is the fluctuating turbulent component,  $l_T$  the turbulent length scale,  $\delta_L$  the flame thickness,  $Da$  the Damköhler number ( $l_T S_L / u' \delta_L$ ), and  $a$  and  $b$  model constants. The constant representing the large-scale turbulence is  $b_1$  while  $b_3$  represents the small-scale turbulence.

### 2.4.1 Damköhler Number

The Damköhler number ( $Da$ ) relates the turbulent timescale ( $\tau_t$ ) to the chemical reaction timescale ( $\tau_c$ ).

$$Da \equiv \frac{\tau_t}{\tau_c} = \frac{l_T/u'}{\delta_L/S_L} \quad (2.19)$$

The integral length scale is calculated in RANS formulation by:

$$l_T = C_\mu^{3/4} \frac{k^{3/2}}{\varepsilon} \quad (2.20)$$

where  $C_\mu = 0.09$ . The flame thermal thickness is calculated through:

$$\delta_L = \frac{\lambda/C_p}{\rho S_L} \quad (2.21)$$

where  $C_p$  is the heat capacity,  $\lambda$  is the molecular conductivity, and  $\rho$  is the density.

When  $Da < 1$ , the flow turbulence time scale is lower than the chemistry rate and the combustion is characterized as diffusion-limited. When  $Da > 1$ , on the other hand, the chemical time scale is smaller than the turbulence time scale, hence the combustion is said to be reaction limited.

### 2.4.2 Karlovitz Number

There are two Karlovitz numbers used in turbulent combustion. When the Kolmogorov scales are used, the Karlovitz number ( $Ka$ ) defines the ratio between the chemical time scale ( $t_c$ ) and the Kolmogorov time scale ( $t_\eta$ ).

$$Ka = \frac{t_c}{t_\eta} = \frac{\delta_L^2}{\eta^2} = \frac{v_\eta^2}{S_L^2} \quad (2.22)$$

where  $\delta_L$  is the flame thickness.  $\eta$  and  $v_\eta$  are the Kolmogorov length and velocity scale, respectively, and are calculated as:

$$\eta = \left(\frac{v^3}{\varepsilon}\right)^{\frac{1}{4}}, v_\eta = (v\varepsilon)^{1/4} \quad (2.23)$$

When Damköhler number is also defined using the Kolmogorov scale,  $Ka = 1/Da$ . When the appropriate reaction zone thickness is used,

$$Ka_\delta = \frac{l_\delta^2}{\eta^2} \quad (2.24)$$

where  $l_\delta$  is the thickness of the inner layer with fraction  $\delta$  of the flame thickness.

Therefore,

$$Ka_\delta = \delta^2 Ka \quad (2.25)$$

When  $Ka > 1$ ,  $Re > 1$ , and  $Ka_\delta < 1$ , the flame is said to be located in the thin reaction zone. When  $Ka < 1$ ,  $Re > 1$ , and  $v' > S_L$ , where  $v'$  denotes the turnover velocity of large eddies, the flame is in the corrugated flamelet regime [9].

## Chapter 3

### Numerical Setup

#### 3.1 1-D Model Setup

The PREMIX model within the Chemkin-pro package [20] was used to calculate the 1-D laminar flame speed. The model assumes a steady, isobaric, quasi-one-dimensional flame propagation. The freely propagating flame speed model was used with mixture-average transport within the entire range of the defined engine-like conditions. This specific model for the flame was used since it calculates the characteristic flame speed of the burnt gas mixture at the specified inlet pressure and temperature.

##### 3.1.1 Boundary Conditions

For a freely propagating flame model, the mass flux is an eigenvalue and must be determined in the solution. The location of the flame is fixed by specifying the temperature at one point ( $x = 0$ ) in a flame-fixed coordinate system.

$$\frac{\partial T}{\partial x} = \frac{\partial Y_k}{\partial x} = 0 \quad (3.1)$$

##### 3.1.2 Chemical Mechanisms

The skeletal GRI 3.0 mechanism by Lu and Law [15] was used as a reference for the calculation of the laminar burning velocity since previous works [3, 5, 7, 18] observed satisfactory predictive modeling of the KAUST data. The Chemkin model used was validated for the selected reduced GRI chemical mechanism by Lu and Law as shown in figure 1.

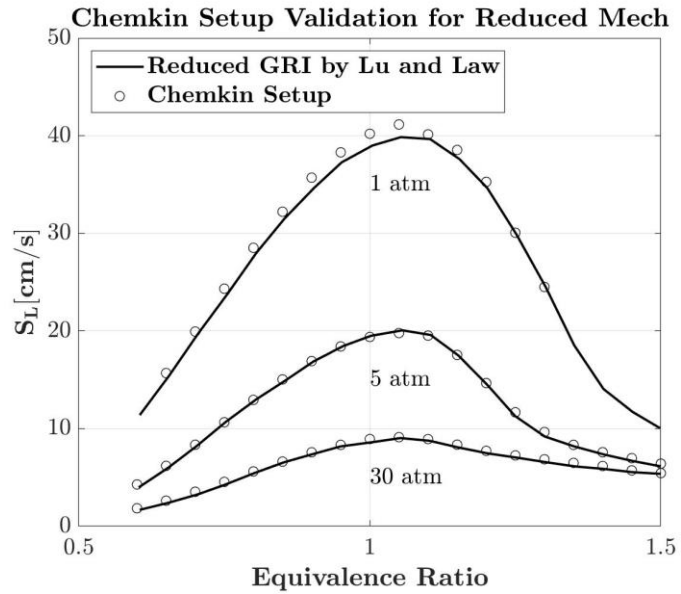


Figure 1: Chemkin setup validation for the reduced GRI mechanism

Using the same freely propagating 1-D premixed laminar flame speed model and setup, the commonly used mechanisms including the reduced and detailed GRI 3.0 [14], Aramco [16], and UCSD [17] mechanisms were compared for the condition of  $T=300$  [K] and  $P=1$  [atm] as further validation of the Chemkin setup used. All mechanisms agree well on the values of  $S_L$  at the ambient condition as shown in figure 2.

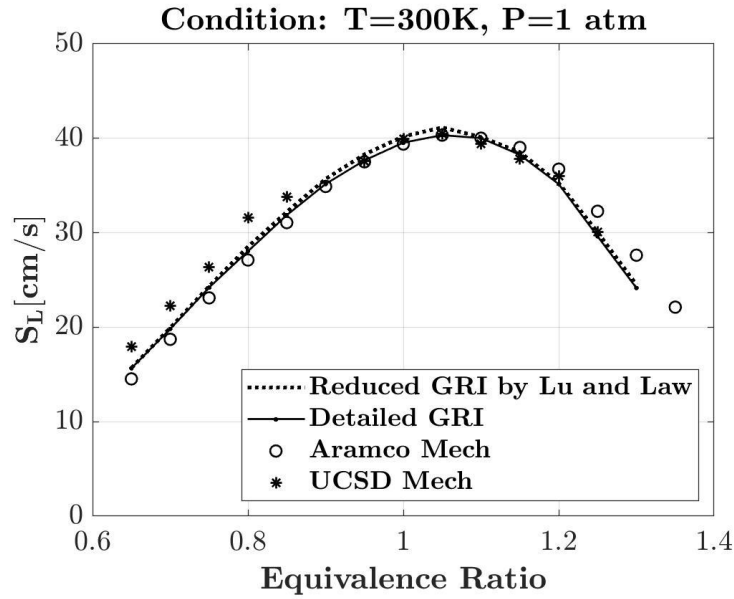


Figure 2:  $S_L$  as determined by various chemical mechanisms at ambient conditions.

### 3.2 CONVERGE setup

The full-scale 3D engine simulations were conducted in the computational fluid dynamics (CFD) solver CONVERGE<sup>TM</sup>. A full-cycle simulation was initially considered. For a balance between saving computational time and adequate field initialization, the solution was mapped at -20 CAD aTDC. The spark timing was -13 CAD aTDC. A homogeneous charge of methane was assumed at the intake port with a global air-fuel ratio  $\lambda = 1.8$ . Three different cases of the same global  $\lambda$  with 3%, 7%, and 13% total fuel energy added in the pre-chamber were investigated.

The grid size for the prechamber region was fixed at 0.25mm. The nozzle connecting the prechamber region and main chamber had grid size of 0.125 mm to

adequately capture the transition between the two chambers. The adaptive mesh refinement (AMR) model was also activated, which generates a smaller mesh size of 500  $\mu\text{m}$  within the main chamber region to maintain a balance between the computational run time and accuracy. The full detailed numerical setup and the KAUST prechamber design can be found in [21].

The turbulence was modeled with the RNG  $k$ - $\epsilon$  model [16]. For combustion modeling, the level set G-Equation model [19] was coupled with the SAGE chemistry solver for the prediction of the intermediate combustion species. Three laminar flame speeds were accounted for in separate simulations: the one tabulated from the skeletal mechanism of GRI 3.0, the original Gulder relation, and the updated Gulder relation. For each of the three cases, three different compositions of the prechamber were investigated: rich, slightly rich, and stoichiometric composition. The turbulent flame speed  $S_T$  was computed using Peters' correlation [18] for all three models.

## Chapter 4

### Optimization and 1-D Flame Speed Assessment

#### 4.1 Gulder's Model Constants

Recall Gulder's correlation for laminar flame speed.

$$S_u(\phi, T, P) = z W \phi^\eta \exp[-\xi(\phi - 1.075)^2] \left[\frac{P_u}{P_o}\right]^\beta \left[\frac{T_u}{T_o}\right]^\alpha \quad (4.1)$$

The three constants that were examined for this work are the temperature exponent  $\alpha$ , and the two empirical constants  $\eta$  and  $\xi$ . The values of the two later constants were originally chosen by Gulder to fit the empirical expression into the experimental data for  $S_L$  of methane at room temperature (300K) and ambient pressure (1atm). Gulder defines the temperature exponent in his  $S_L$  correlation to be in the range of 1.37 to 2.33 for methane at various equivalence ratios and pressures [11]. While the value of the pressure exponent  $\beta$  is agreed to be -0.5 for methane, the value of the temperature exponent is still argued within the combustion community [12, 13, 22-24]. Usual engineering practices that utilize Gulder's model assume a value of  $\alpha = 2$  for methane. However, within the  $\alpha$  range suggested by Gulder,  $S_L$  can vary significantly at high pressures as shown in figure 3. As observed, the choice of the value for  $\alpha$  can greatly affect the value of Gulder's  $S_L$ .

Previous works have investigated the value of the temperature exponent and its dependence on pressure and equivalence ratio. Babkin and Kozachenko [13] explored the effect of high pressure and temperature on mixtures containing methane. They found that while the pressure exponent is also a function of temperature and mixture composition, it

is almost constant for pressures higher than 8 [atm] [13]. As for the temperature exponent, they state that  $\alpha$  has a minimum value of 2 near stoichiometry, but its value is not constant for rich and lean mixtures and at higher pressures. It is also mentioned in their work that within the pressure range of 1-70 atm, the value of temperature exponent increases from 2.32 to 3.01 for an methane-air mixture containing 8% methane. Since  $\alpha$  denotes the slope of the corresponding curve of  $S_L \sim T^\alpha$ , they calculate the temperature exponent according to:

$$\alpha = \frac{\log(S_{u_2}/S_{u_1})}{\log(T_{i_2}/T_{i_1})}, \quad (4.2)$$

where  $S_{u_2}$  and  $S_{u_1}$  are the normal burning velocities at two different states of the same mixture, and  $T_{i_2}$  and  $T_{i_1}$  are the temperatures of the fresh mixture at the respective states. Babkin's calculation of  $S_L$ , and consequently  $\alpha$ , is done relatively between two different states: ambient (state 1) and another state where the temperature and pressure are usually higher (state 2). Furthermore, they state that the quantity  $(S_{u_2}/S_{u_1})$  is a function of  $\sqrt{n_{b_2}/n_{b_1}}$ , the ratio between the two relative mass concentrations of the chain carriers (H, O, and OH) at the two combustion temperatures  $T_{b_1}$  and  $T_{b_2}$ . The method of successive approximation for weak dissociation was used to calculate the chain carrier concentrations [13]. Therefore, an increase in pressure results in a decrease in the degree of dissociation, which leads to enhancing the efficiency of heating. According to their experimental calculation of the heating efficiency and  $\sqrt{n_{b_2}/n_{b_1}}$ , an increase in efficiency results in an increase in  $\sqrt{n_{b_2}/n_{b_1}}$ ; hence, an increase in  $\alpha$ . Therefore, operating at high pressures requires a higher value for the temperature exponent than that suggested by Gulder since

the prechamber engine operates at much higher temperature and pressure than that investigated by Gulder [11].

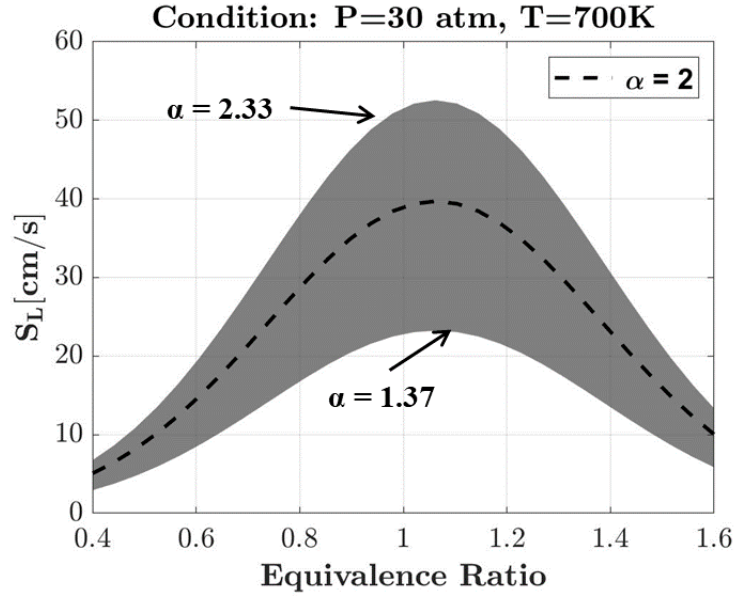


Figure 3: Variation in Gulder's  $S_L$  within the Gulder's range of  $\alpha$  at high pressure and temperature

Varghese et al [23] used the method of an externally heated diverging channel that accurately measures the laminar flame speed to evaluate the joint effect of high pressure and temperature on the propagation of premixed methane-air flames within the range of  $\phi = 0.7 - 1.3$ ,  $P = 1 - 5 \text{ atm}$ , and  $T = 350 - 650 \text{ K}$ . They confirm the dependence of the temperature exponent on pressure and report that  $\alpha = \alpha_0 + \alpha_1 \left(1 - \frac{P_u}{P_{u,0}}\right)$  where  $P_{u,0} = 1 \text{ [atm]}$  and  $\alpha_0$  and  $\alpha_1$  are the coefficients of linear fit whose values depend on the mixture composition. Their expression for  $\alpha$  was determined by a linear fit of the variation of the temperature exponent at various pressures. Their experimental results for the variation in

$\alpha$  were compared, with a fair agreement, to the prediction of  $S_L$  according to the Aramco 2 kinetic mechanism. Clearly, the value of  $\alpha$  in Gulder's correlation must be selected to reflect engine-like conditions of high pressure and temperature.

Similarly, the values of the constants  $\eta$  and  $\xi$  are fuel-dependent and were selected to fit Gulder's experimental data at ambient temperature and pressure. Therefore, adjusting them to fit higher pressure and temperature conditions can result in the desired change in the calculation of Gulder's  $S_L$  at high pressure and temperature.

## 4.2 Constants Optimization Method

After selecting the three constants in Gulder's model that is to be adjusted, a simple method of optimization was followed to select the new values of such constants. The approach adopted was to systematically minimize the difference between the  $S_L$  calculated from Gulder and the  $S_L$  from skeletal GRI. This was done for the full range of engine conditions defined as  $\phi = 0.6 - 1.5$ ,  $P = 30 - 80 atm$ , and  $T = 700 - 1060 K$ . This means that the new values of the constants were optimized such that Gulder's prediction of  $S_L$  matches the GRI mechanism's  $S_L$ . The global minimum was obtained by:

$$\% \text{ diff} = \frac{S_{L,Gulder} - S_{L,GRI}}{S_{L,GRI}} \quad (4.2)$$

$$\text{Total Average \% diff} = \frac{\sum_P \sum_T \sum_\phi \% \text{ diff}}{\# \text{ of points in engine conditions range}} \quad (4.3)$$

The original values of  $\alpha$ ,  $\eta$ , and  $\xi$  were separately doubled and halved to assess their sensitivity and be used as a range from which the new optimized values will be

selected. For each constant, the Gulder's  $S_L$  was calculated as a function of the constant within its respective range. Then, the individual percent difference between Gulder's  $S_L$  and the GRI's was calculated according to (4.2). The final optimized value for each constant was selected to minimize (4.3). Figure 4 shows the optimization of the temperature exponent  $\alpha$ . Within the range of  $\alpha = 1 - 4$ , the percent difference between the two  $S_L$ 's at each point in the engine conditions range was calculated. Finally, the value of  $\alpha$  that minimized the total average percent difference between Gulder's  $S_L$  and the chemical mechanism's  $S_L$  as calculated by (4.3) was then selected. The process was identical for the other two constants. Optimal values of 2.6, 3.94, and 0.273 were found for  $\alpha$ ,  $\xi$ , and  $\eta$ , respectively.

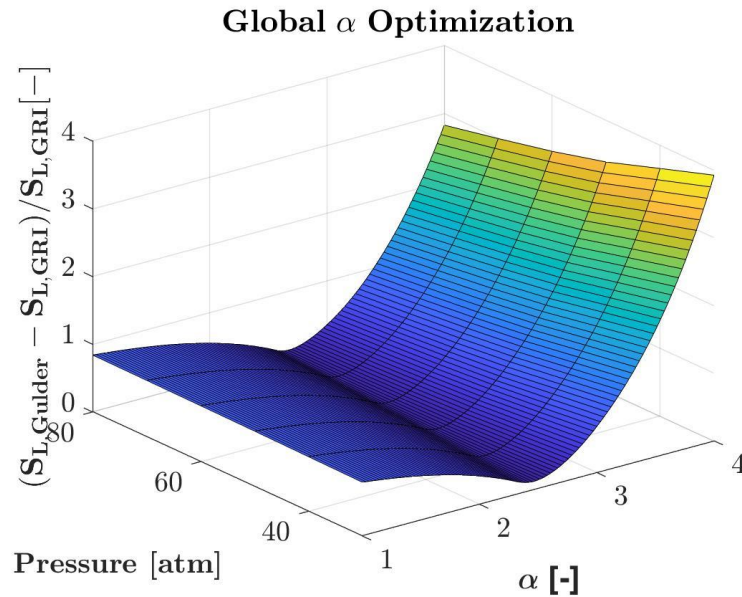


Figure 4: Percent difference between the two  $S_L$  for the range of  $\alpha = 1 - 4$ .

## 4.2 1-D Laminar Flame Assessment

The effect of the optimized values within Gulder's updated model was tested in 1-D Chemkin simulations by comparing Gulder's  $S_L$  to the GRI's. Figure 5 shows the comparison between the  $S_L$  computed from the reduced GRI mechanism and Gulder's original model for a representative pressure of 40 [bar], while figure 6 compares the updated Gulder relation against the reference  $S_L$ . It is clear from the figure that Gulder's original relation for the laminar burning velocity calculated significantly lower values than those calculated using the reduced GRI 3.0. Although not shown here, the mismatch in calculation of  $S_L$  is observed in all the range of pressure investigated for this work.

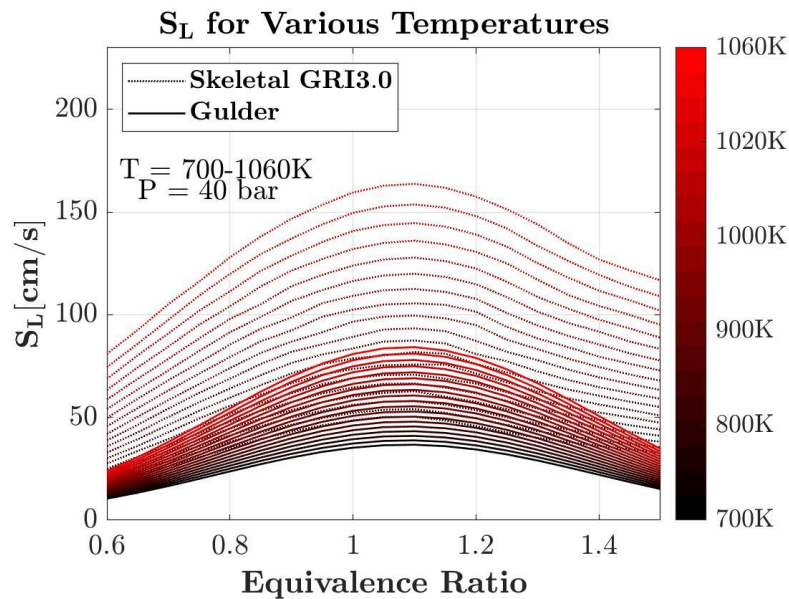


Figure 5:  $S_L$  - Gulder vs. skeletal GRI – for a wide temperature range and  
P=40atm

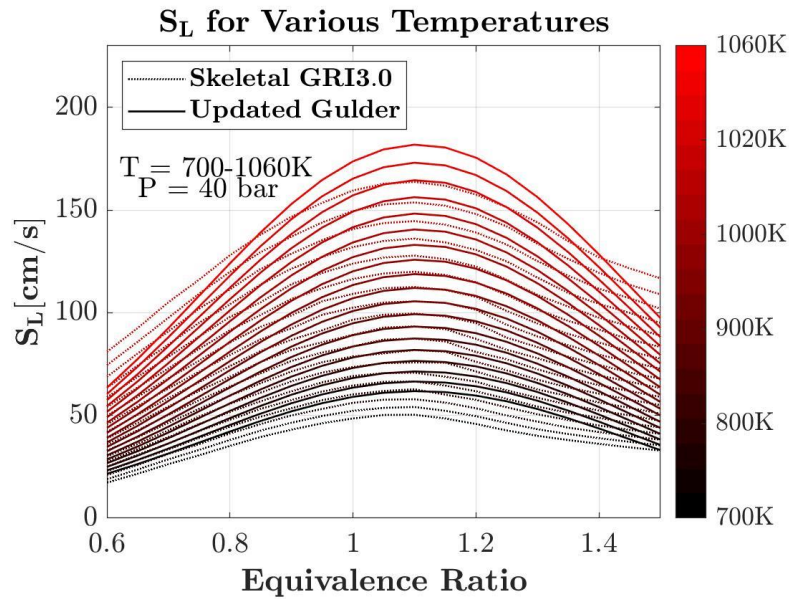


Figure 6:  $S_L$  – updated Gulder vs. skeletal GRI - for wide temperature range and  $P=40\text{atm}$

Using the optimized values of Gulder’s constants improves the agreement between the empirical flame velocity model and the baseline case that utilizes the reduced GRI mechanism. Although the curves are not identical, the magnitude of the flame speed is more similar between the updated model and the reference case than between the original model and the baseline case. Due to the global averaging of the optimized constants over a wide range of engine conditions, the updated model still differs from the reference mechanism.

It is possible to minimize the difference between the curves even further by suggesting temperature, pressure, or equivalence ratio-dependent values for the investigated constants. However, this work aims to introduce as minimal a change to Gulder’s original model as possible for easier implementation in the CFD solver

CONVERGE. Therefore, the small remaining difference between Gulder's  $S_L$  and the mechanism's is considered acceptable for this work.

## 4.2 Summary

It was shown that the values for Gulder's empirical constants for methane are heavily dependent on the operating temperature, pressure, and composition. The temperature exponent, specifically, has been studied in many works. All such efforts agree with Babkin's explanation for the relationship between the temperature exponent and pressure [12, 13, 22-24]. Babkin's work shows that the temperature exponent value must be more than 2 for pressures higher than 1 [atm], and it increases with increased pressure [12, 13, 22-24]. The original values suggested by Gulder for those constants, therefore, are not applicable for the high temperature and pressure and ultra-lean engine conditions since they were selected to fit the correlation into his experimental data gathered at ambient temperature and pressure.

For Gulder's relation to correctly predict the laminar flame speed for such extreme conditions, its empirical constants were adjusted. Using the calculations of the laminar burning velocity from the skeletal GRI 3.0 chemical mechanism as a reference, the constants were altered so the Gulder's correlation would calculate similar  $S_L$ . The constants were optimized for a global average minimum difference between the Gulder's and the mechanism's  $S_L$ . The optimized relation was then implemented in Chemkin for 1-D flame speed assessment. The 1-D results show a significant improvement in the magnitude of  $S_L$  as calculated by the updated correlation and compared to the reference  $S_L$ .

## Chapter 5

### 3D CFD Results

#### 5.1 Effect of Updated Laminar Burning Velocity

To assess the effect of the new optimized constants, the updated Gulder's model was implemented in CONVERGE. Figure 7 shows the CFD results of the three prechamber combustion models that utilize laminar flame speeds computed from the skeletal GRI 3.0 (Fig. 7 (a)), original Gulder (Fig. 7 (b)), and modified Gulder (Fig. 7 (c)), with 3% of the total fuel energy added in the prechamber. All three models are compared to the average KAUST experimental engine data shown in black. The individual experimental cycles are shown in grey. The in-cylinder pressure measurement is used as a reference to analyze the combustion process quantitatively and evaluate the predictability of each combustion model. The running time for the models that use the empirical expressions is around 20% less than that of the model using the tabulated data. The 3D flame topology for all three cases are shown at two different positions: when the jet hits the piston wall and at TDC. These two critical positions in flame development were selected to highlight the differences that result from the three different models.

After flame initiation in the prechamber, the flame starts to propagate and the pressure in the prechamber then increases. When the prechamber pressure surpasses that of the main chamber, the flame is passed into the main chamber through the connecting nozzles as highly reactive jets. The shear-driven instabilities cause the wrinkling of the

flame front and the development of a mixing layer, which maintains the combustion of the homogenous charge in the main chamber until all the jets have passed from the prechamber.

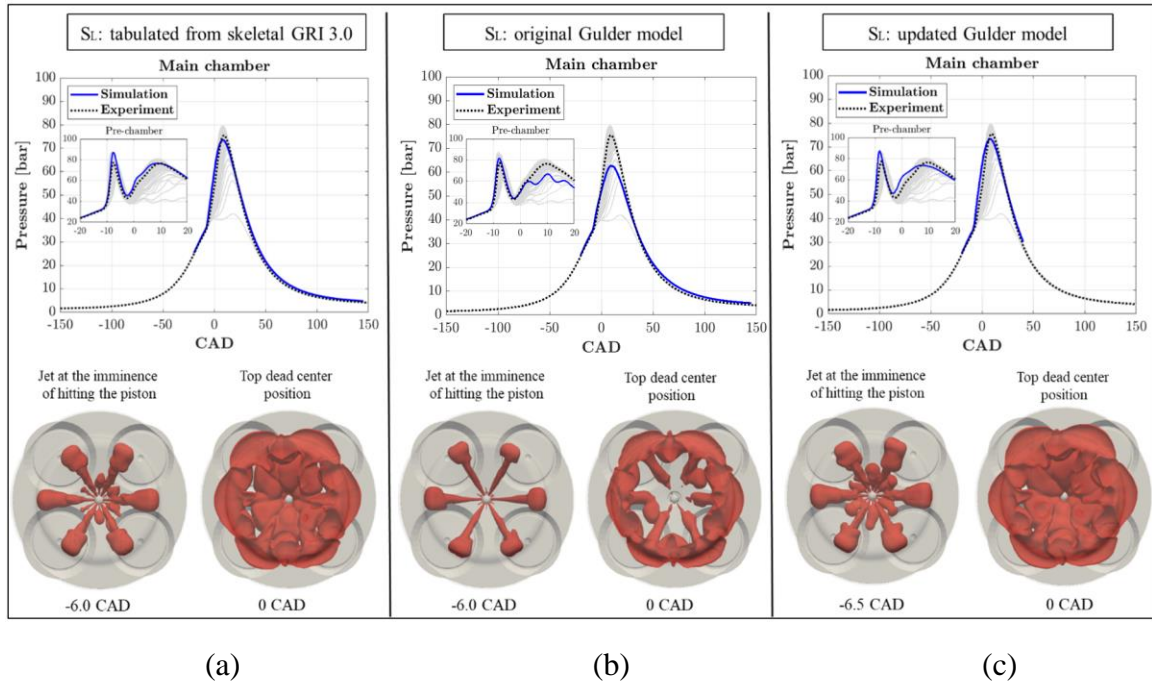


Figure 7: CFD and 3D results for tabulated mechanism and Gulder's original and updated models with PCFR 3%

Figure 7 (a), which utilizes the  $S_L$  calculation from the skeletal GRI3.0, shows a satisfactory agreement with the experimental results and is, therefore, used as a reference. Gulder's original model (Fig. 7 (b)) does not show an acceptable agreement with the experimental results nor the 3D reference flame topology. When the flame enters the main chamber, its cross-sectional development is poor compared to the baseline case. Gulder's original model underpredicts the peak pressure in the main chamber by 13% in this case. While it predicts the maximum pressure in the prechamber well, the original model's prediction after TDC is less consistent with the average experimental data. This inconsistency between Gulder's model and the experimental results has been observed in

other works [8]. In those works, the mismatch was believed to result from the calculation of the turbulent flame speed. To resolve the mismatch, Kim et al [8] altered the model constants  $b_1$  and  $b_3$  in Peters' correlation of  $S_T$  from 2.0 and 1.0 to 1.5 and 2.0, respectively. The adjusted values were chosen such that the simulated maximum pressure in the main chamber match the experimental one [8].

In fact, the mismatch could not be turbulence-driven, since Peters' turbulent flame speed correlation is used for all three cases shown in figure 7. The only difference among the three combustion models is the laminar burning velocity. Therefore, the mismatch in figure 7 (b) must be due to the slow laminar flame speed. The slow laminar flame speed, in fact, compromises the propagation of the turbulent flame, the flame surface area, and the mean pressure prediction in the case of Gulder's original model.

Furthermore, the value of the constant model  $b_3$ , according to Peters, was not selected to fit the correlation into experimental data the same way the adjusted Gulder's model constants were [9]. Instead, it was derived by Damköhler (1940) from the relation  $S_T/S_L = b_3\sqrt{D_t/D}$ , where  $D$  is the molecular diffusivity and  $D_t$  the turbulent diffusivity, and was confirmed through direct numerical simulations (DNS) conducted by Wenzel in 1997 [9]. Therefore, the value of  $b_3$  must not be modified arbitrarily without solid physical reasoning.

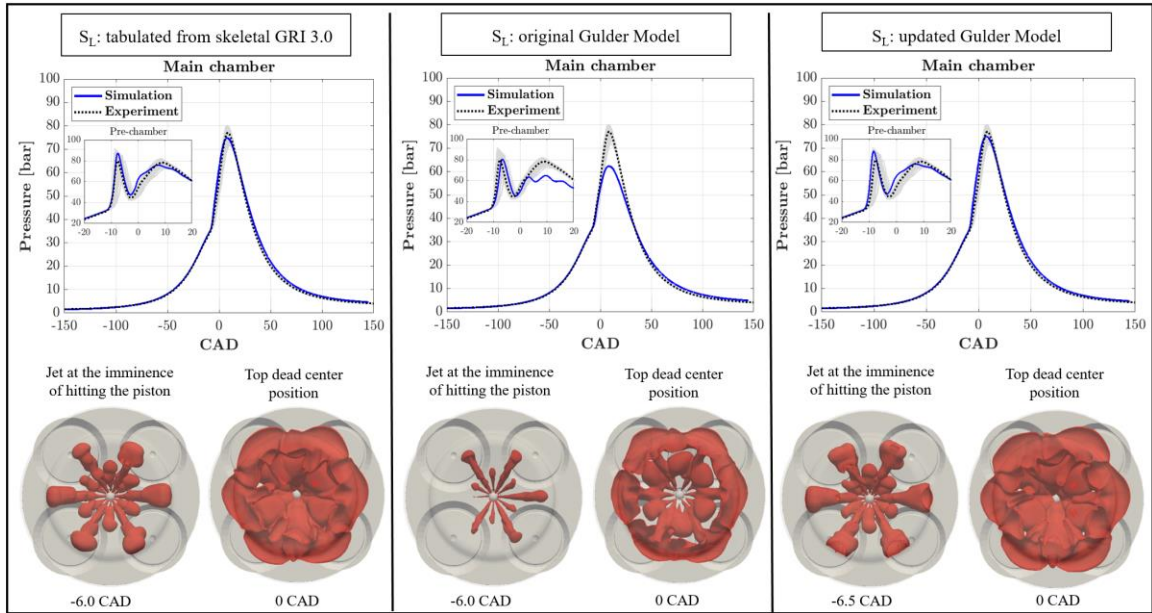
Gulder's updated model (Fig. 7 (c)) shows significant improvement compared to the performance of Gulder's original model. The updated model predicts the average pressure profile well in both the pre and main chambers. This improvement confirms the earlier claim that the mismatch between Gulder's original model and the experimental

results is due to the inaccurate prediction of the laminar flame speed instead of the turbulent flame speed. The mismatch still present between the updated Gulder model and the experimental results is considered negligible and is an expected outcome of the global averaging of the optimized constants. However, the 3D flame topology of the updated model agrees well with the baseline case as compared to the original model. The slight difference of 0.5 in the crank angle in the case of the updated Gulder model for the flame topology at the jet hitting the piston is considered minor compared to the improvement obtained.

It is critical to mention that the still remaining difference seen in figure 7 (c) can be further minimized by optimizing the values of  $\alpha$ ,  $\eta$ , and  $\xi$  for specific local conditions (for a given  $P$ ,  $T$ ,  $\phi$ ). Future work could be dedicated to investigate a dynamic optimization of the constants as a function of the local rather than the global conditions.

To further confirm the applicability of Gulder's updated model, additional assessments with PCFR 7% and 13% were conducted and shown in figure 8 and figure 9, respectively. Similar to the case of PCFR 3%, Gulder's model (Fig. 8 (b)) fails to predict the pressure profile in the prechamber and main chamber after TDC. Its flame topology also shows a significant lag, when compared to the baseline case (Fig. 8 (a)), in the jets issued from the prechamber. The updated Gulder's model (Fig. 8 (c)), on the other hand, predicts both pressure profiles in the main and prechamber significantly well. Notice that although the prechamber peak pressure predicted by the updated model is slightly higher than the average experimental peak pressure, it still falls within the range of maximum pressure in the experimental cycles. The flame development of the updated model agrees

well with the reference case in both cross-sections shown with a slight, but expected difference.



(a)

(b)

(c)

Figure 8: CFD and 3D results for tabulated mechanism and Gulder's original and updated models with PCFR 7%

The patterns discussed in figure 7 and figure 8 are also observed in figure 9. The updated model performs better than the original model in both predicting the pressure profiles and the flame development. With 13% of the fuel energy added into the prechamber, a rich homogenous charge is available in the prechamber. It is considered an extreme case compared to the near-stoichiometric and slightly rich cases of PCFR 3% and 7%. That explains why both the reference case and the updated model predict a slightly

smaller peak pressure than the average experimental maximum pressure in the main chamber.

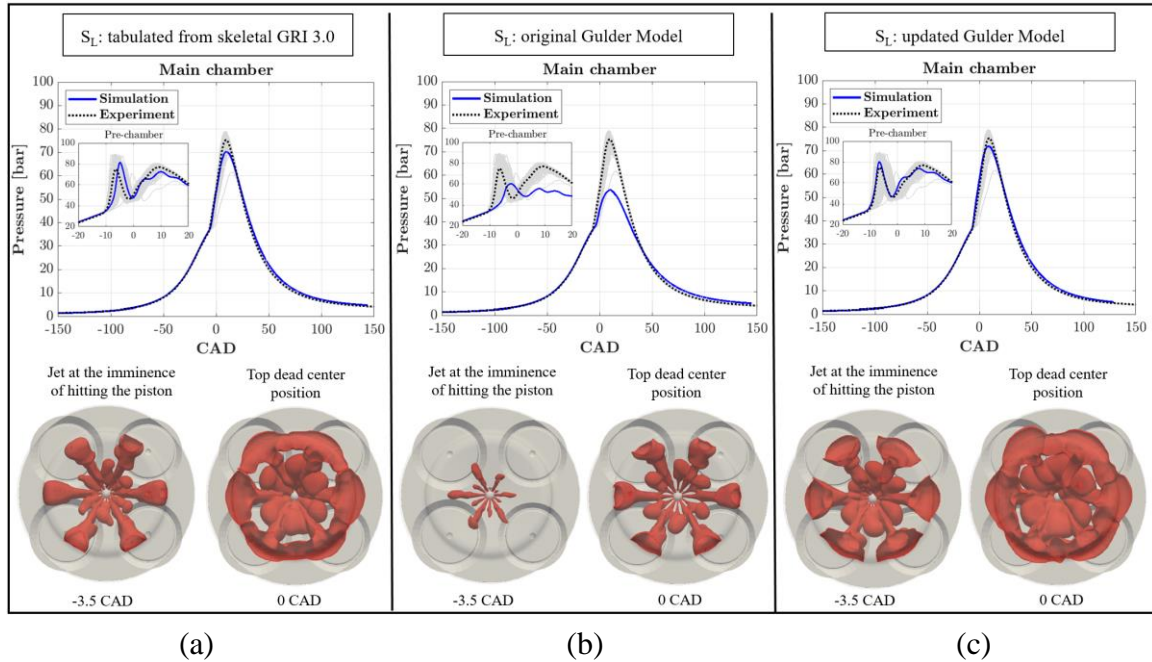


Figure 9: CFD and 3D results for tabulated mechanism and Gulder's original and updated models with PCFR 13%

In both cases, however, the predicted pressure still falls within the range of the experimental peak pressure, unlike the peak pressure predicted by Gulder's original model (Fig. 9 (c)). Furthermore, Gulder's updated model's prediction of the flame development at -3.5 CAD appears faster than the prediction provided by the baseline case. This is consistent with the difference in the peak pressures as calculated by the two models. Recall that in figure 6, the updated model calculates slightly faster  $S_L$  at stoichiometric and slightly rich equivalence ratios. Therefore, it is expected that the optimized model's flame develops faster than the reference case.

## 5.2 Analysis of Damköhler Number and Borghi-Peters Diagram in Pre and Main Chambers

One critical observation seen in figure 7 and figure 8 is that minimal perturbation of the prechamber pressure builds up irrespective of the  $S_L$  used, while the main chamber is heavily affected. In the case of PCFR 13%, however, a different pattern is observed. Gulder's original model completely fails to predict the pressure in the prechamber. This section provides a priori reasoning for such observations of prechamber pressure prediction.

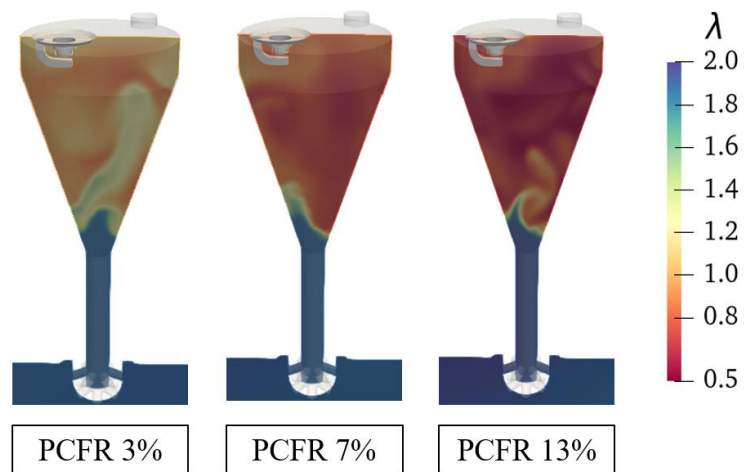


Figure 10: 3D results of the prechamber composition at spark time (-13 CAD)

### 5.2.1 PCFR 3%

The prechamber composition for a PCFR of 3% is around stoichiometry. It can be observed in figure 7 that updating Gulder's model, and hence changing the calculation of  $S_L$ , does not significantly alter the prediction of the prechamber pressure prior to TDC. Figure 11 shows the prechamber pressure as predicted by the three models for the case of PCFR 3%. Gulder's original model seems to acceptably predict the average prechamber pressure up to TDC. After TDC, the original model's prediction of prechamber pressure is less consistent with the average experimental data and baseline case but still falls within the range of experimental cycles. The updated model consistently matches the reference case throughout the entire the combustion process.

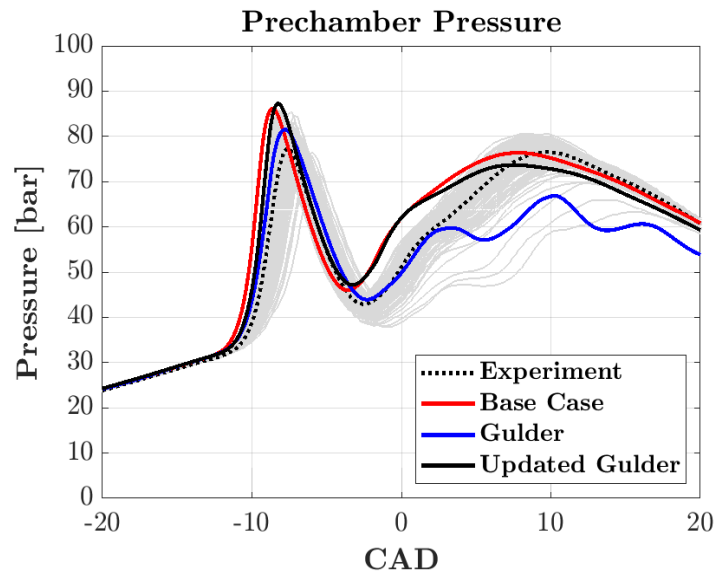


Figure 11: Prechamber pressure as predicted by the reference case, Gulder's original model, and Gulder's updated model for the case of PCFR 3%

The flame topology within the prechamber region shown in figure 12 for all three models is in fair agreement. The effect of Gulder's slow  $S_L$ , however, is clear in the analysis of Damköhler number. Recall that Damköhler number is a function of the laminar burning velocity. Gulder's slower flame speed, therefore, corresponds to smaller Damköhler numbers in the prechamber region. The effect of the slow speed on the flame development becomes more apparent when the flame enters the main chamber. The 3D results for the prechamber agree with the pressure prediction shown in figure 11. Gulder's original model produces acceptable results for the prechamber before TDC.

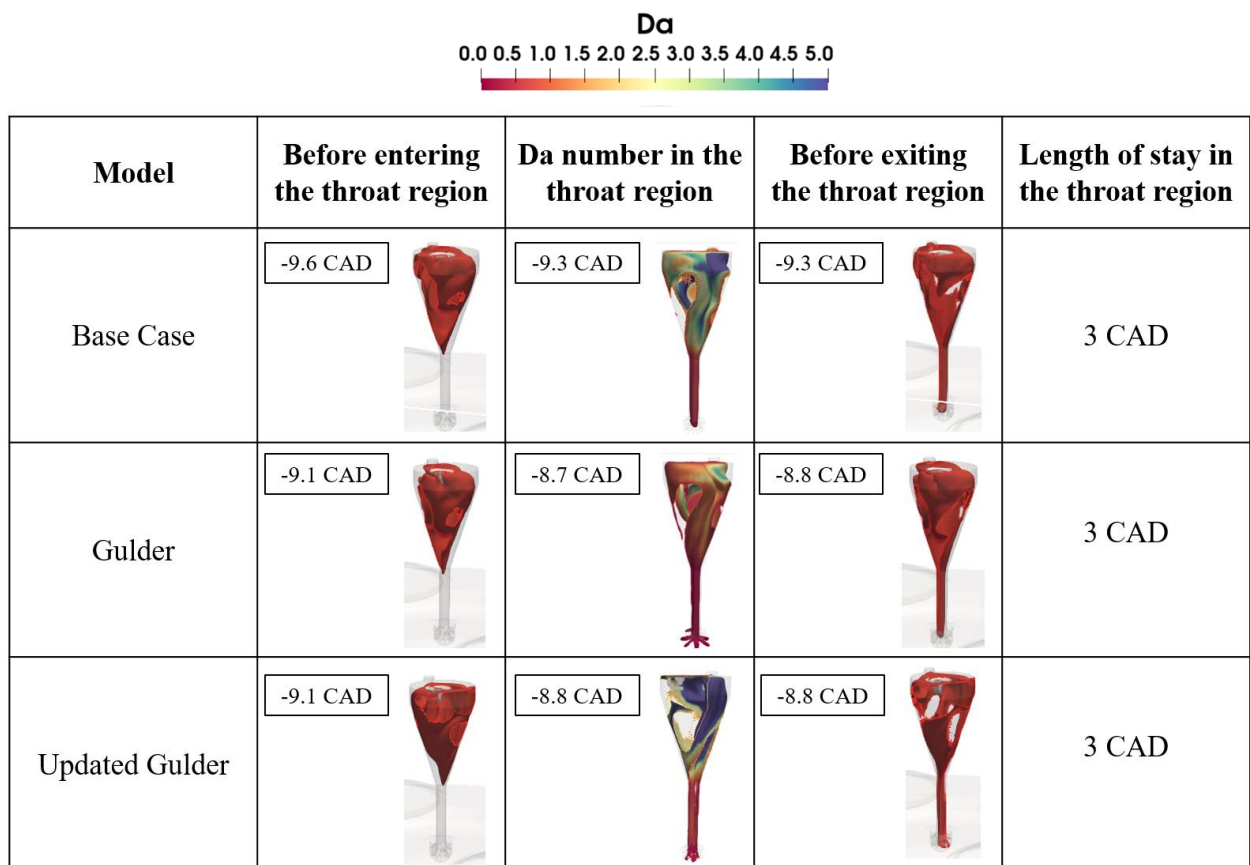


Figure 12: 3D results of flame topology and Damköhler number within the prechamber region for the three models for the case of PCFR 3%

Similar to the prechamber pressure, the main chamber pressure as predicted by Gulder's model agrees with the average experimental and reference curves before TDC. Even though the model predicts a pressure within the range of the experimental cycles after TDC, it doesn't match the baseline case. The 3D results of the jets development for the three models show a great disagreement. Even prior to TDC, the slow flame speed calculated by Gulder's original model is clearly observed in the main chamber. Its effect compromises the jets development as the flame enters the main chamber and after the jets hit the piston walls. The average Damköhler number, for the reference case and the updated model, recovers to be larger than unity once the jets hit the piston walls and the turbulent mixing starts. In the case of Gulder's original model, due to the slow  $S_L$ , the average Damköhler number stays less than one. The turbulent mixing of the flame at TDC is also compromised due to the poor development of the turbulent jets. The updated model predicts better jets development and turbulent mixing; hence the agreement on the pressure profile in the main chamber between the updated model and the baseline.

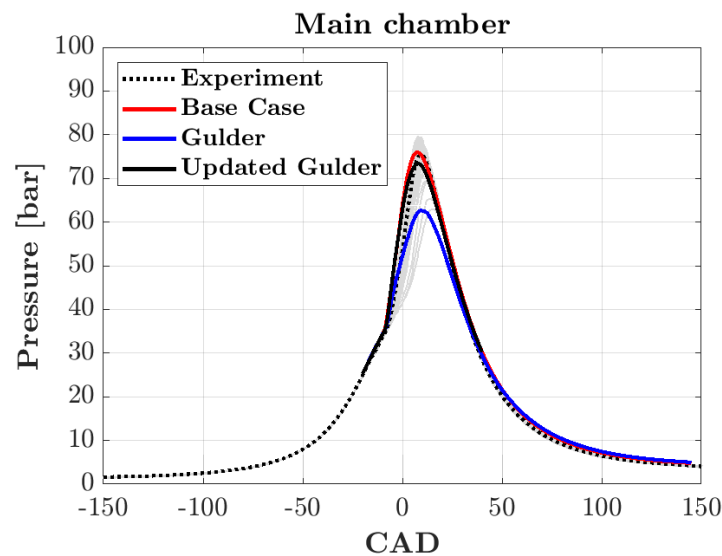


Figure 13: Main chamber pressure predicted by the reference case, Gulder's original model, and Gulder's updated model for the case of PCFR 3%

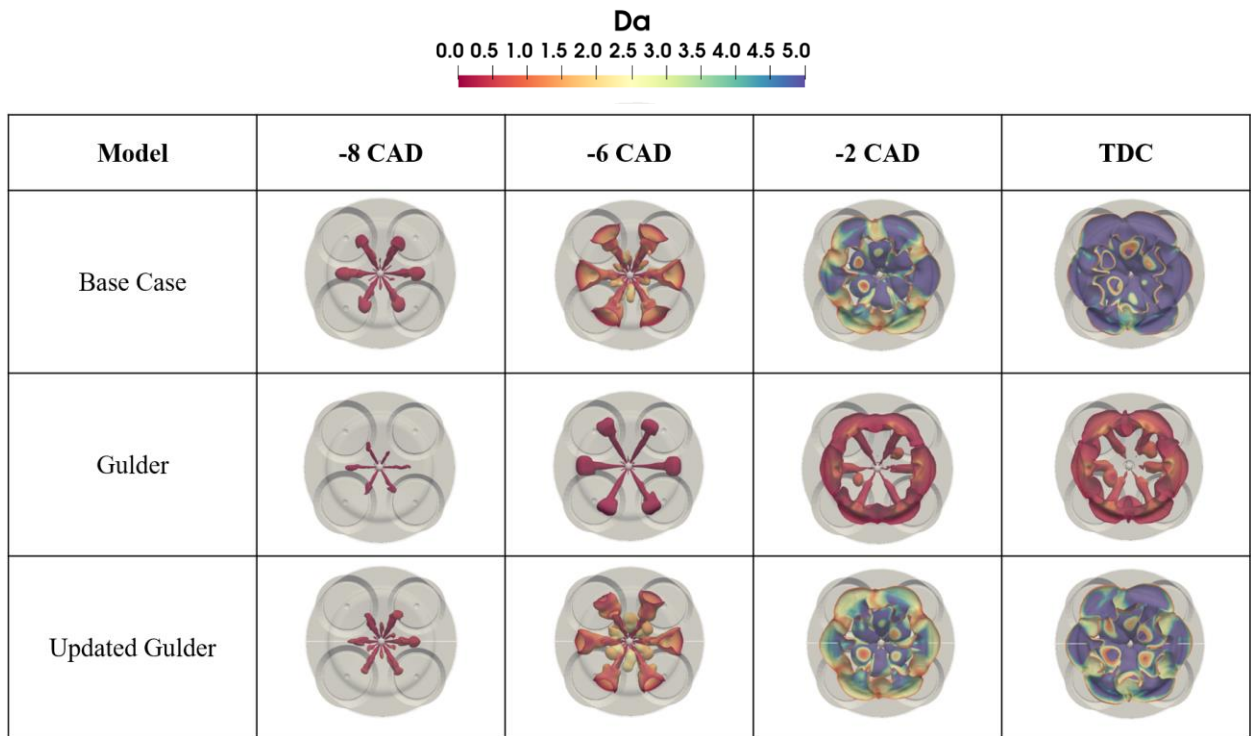


Figure 14: 3D results of flame topology and Damköhler number within the main chamber region for the three models for the case of PCFR 3%

Both behaviors observed for Gulder's original model in the prechamber and main chamber regions can be explained by examining the Borghi-Peters diagram shown in figure 15. The diagram shows the simulation data points taken ahead of the flame. For the baseline case, the flame starts in the thin reaction zone and transfers to the corrugated flamelet regime right after TDC. It is critical to note that in the corrugated flamelet regime, the Karlovitz number is less than unity and the laminar flame speed is similar in magnitude to the turbulent fluctuations [9]. Recall that Peters' correlation calculates the turbulent flame speed as a combination of the laminar flame speed and the turbulent fluctuations [9]. Therefore, the effect of  $S_L$  becomes more significant while calculating  $S_T$  when the flame

is in the corrugated flamelet regime than when it is in the thin reaction zone. Furthermore, the slow laminar flame speed calculated by Gulder's original model results in a sufficiently large  $u'/S_L$  ratio that the flame enters the broken reaction zone, where the G-equation is not valid [9]. This explains why Gulder's original model fails after TDC.

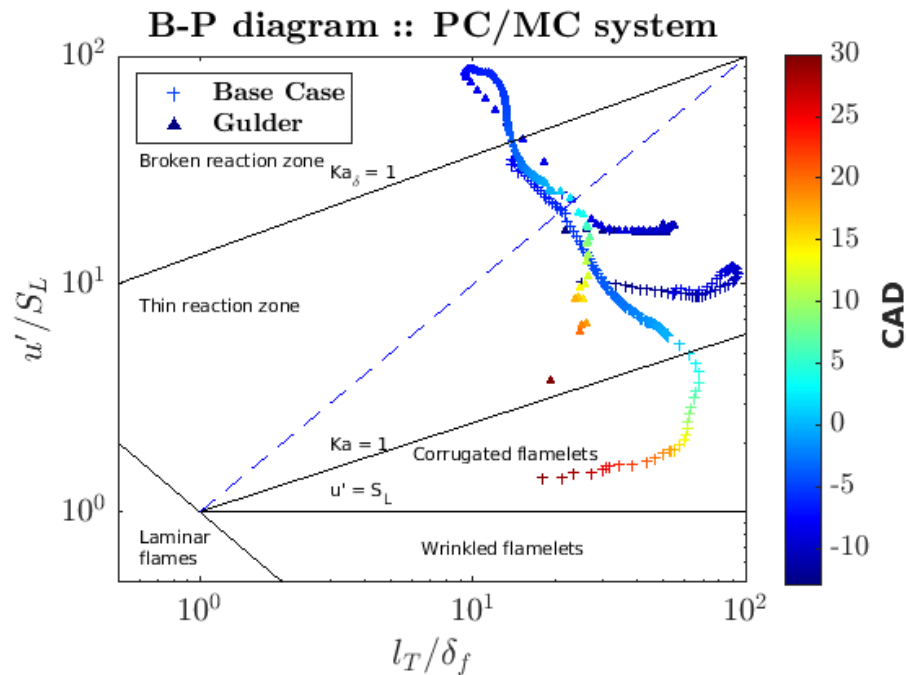


Figure 15: Borghi-Peters diagram for PCFR 3% showing the base case and Gulder's original model

Figure 16 shows that the updated model is in good agreement with the reference case in terms of the flame front location in the Borghi-Peters diagram. Both flame fronts start in the thin reaction zone and transfer into the corrugated flamelet regime around TDC. When  $S_L$  is calculated using Gulder's updated correlation, the  $u'/S_L$  ratio is not too large that the flame front enters the broken reaction zone. The slight differences observed again

result from the global averaging of the model constants explained in chapter 4. In addition, the difference in the flame front data is consistent with the difference seen in figure 6 and figure 12. Recall that in figure 6, the optimized model slightly overpredicts  $S_L$  compared to the reference case at stoichiometric and slightly rich equivalence ratios. This difference causes a faster increase in the pressure predicted by the updated model compared to the reference case observed in figure 12. Note that by 30 CAD, the combustion process is considered complete. Therefore, the points in the case of the updated model that enter the wrinkled flamelet regime are of no major significance to the validity of the optimized Gulder's model.

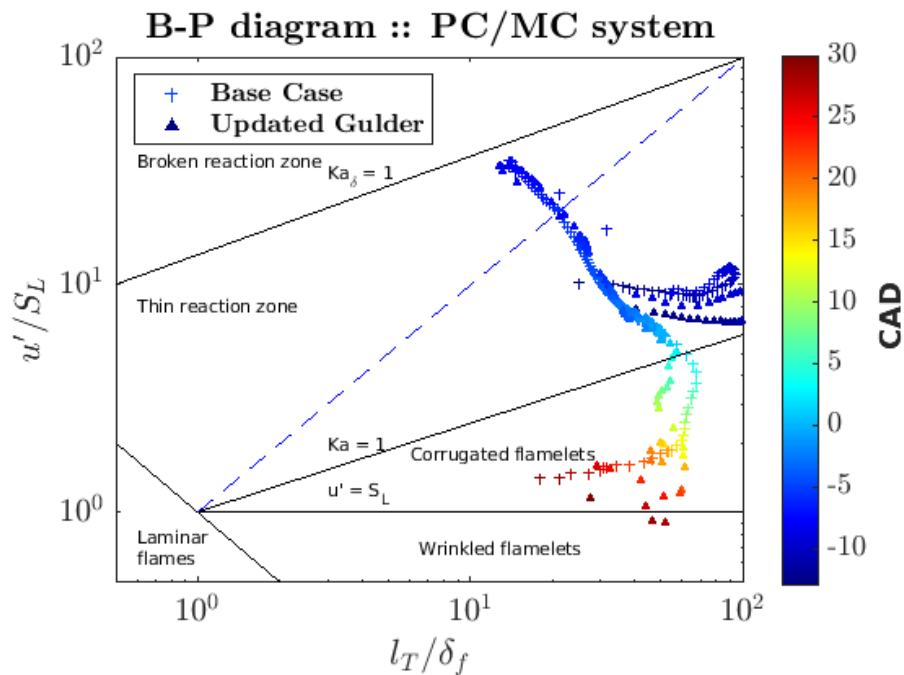


Figure 16: Borghi-Peters diagram for PCFR 3% showing the base case and Gulder's updated model

### 5.2.2 PCFR 7%

For a PCFR of 7%, the prechamber composition corresponds to a slightly rich mixture of  $\lambda = 0.8$  on average as seen in figure 10. The same pattern explained for the prechamber pressure prediction of PCFR 3% is observed here. Gulder's original model acceptably predicts the prechamber pressure only before TDC. After TDC, in the case of PCFR 7%, the pressure predicted by the original model falls outside the range of the pressures obtained in the experimental cycles. The agreement between the baseline and the updated model is seen again here.

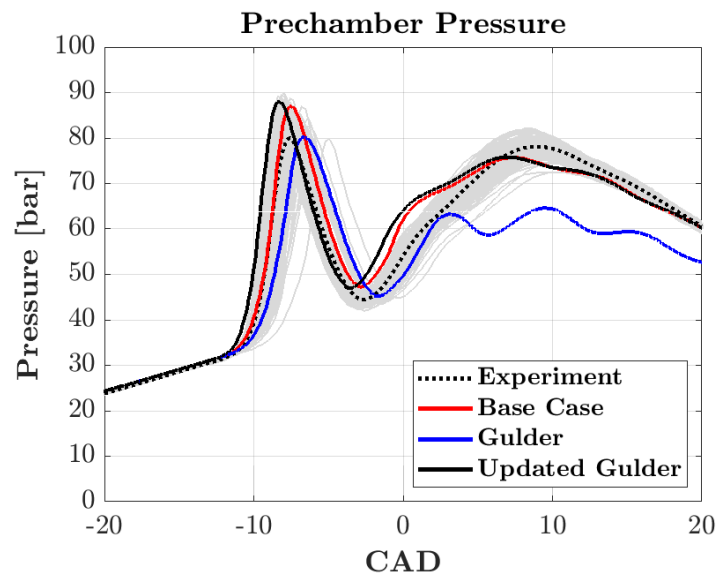


Figure 17: Prechamber pressure as predicted by the reference case, Gulder's original model, and Gulder's updated model for the case of PCFR 7%

Figure 18 shows the flame development at -11 CAD for all three models. Clearly, Gulder's original model flame develops slower than the reference case and the updated

model. This delay, however, does not cause a significant disagreement in the pressure profile before TDC. The delay in  $S_L$  seems to build up cumulatively over time in the prechamber, and the lag becomes more evident in the flame topology by the time the flame exits the prechamber. Since the effect of the slow speed is more dominant in the flame development in the case of the 7% than in the 3%, Gulder's original model's prediction of the prechamber pressure in figure 17 has a slower rate of increase when compared to the reference case while it does not in figure 11. The slower  $S_L$  again results in smaller Damköhler numbers in the prechamber as seen in the previous case.

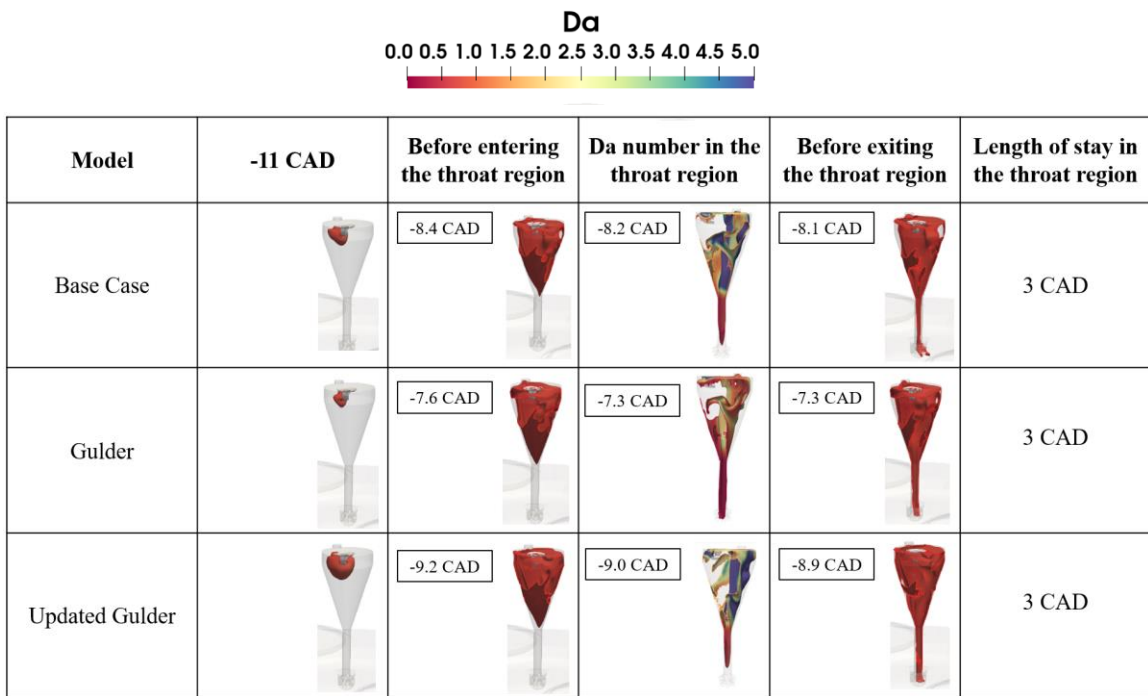


Figure 18: 3D results of flame topology and Damköhler number within the prechamber region for the three models for the case of PCFR 7%

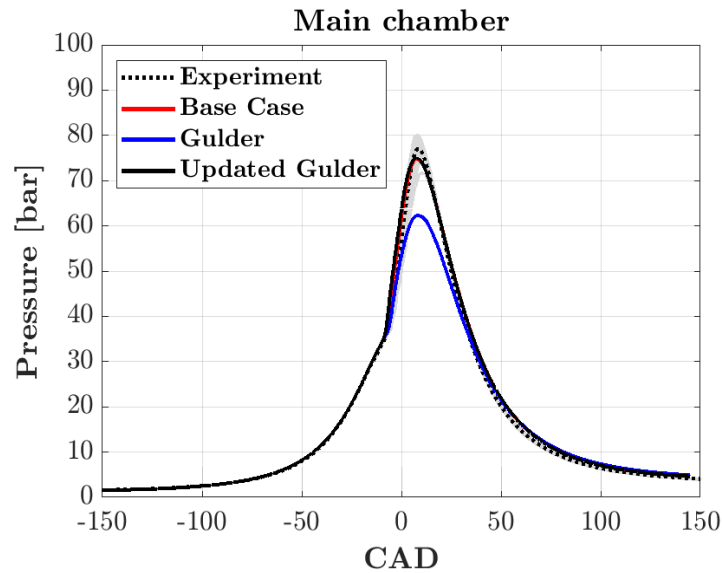


Figure 19: Main chamber pressure as predicted by the reference case, Gulder's original model, and Gulder's updated model for the case of PCFR 7%

Figure 19 shows the main chamber pressure as predicted by the three models for PCFR of 7%. Similar to the case of PCFR 3%, Gulder's original model predicts the pressure profile well within the main chamber region before TDC but significantly fails starting at TDC and until the end of the combustion process around 30 CAD. Figure 20 shows the flame development in the main chamber and the Damköhler numbers for the three models. The slow Gulder's flame compromises the jets development in the main chamber. In addition to entering the main chamber later than the reference case, Gulder's slow flame results in smaller Damköhler numbers even at TDC. The poor development of the jets also results in poor turbulence at TDC when compared to the reference case and the updated model. The updated model, on the other hand, calculates sufficiently fast laminar flame speed that both the flame development and Damköhler numbers match the reference case despite the slight advancement of the flame seen in figure 18 and figure 20.

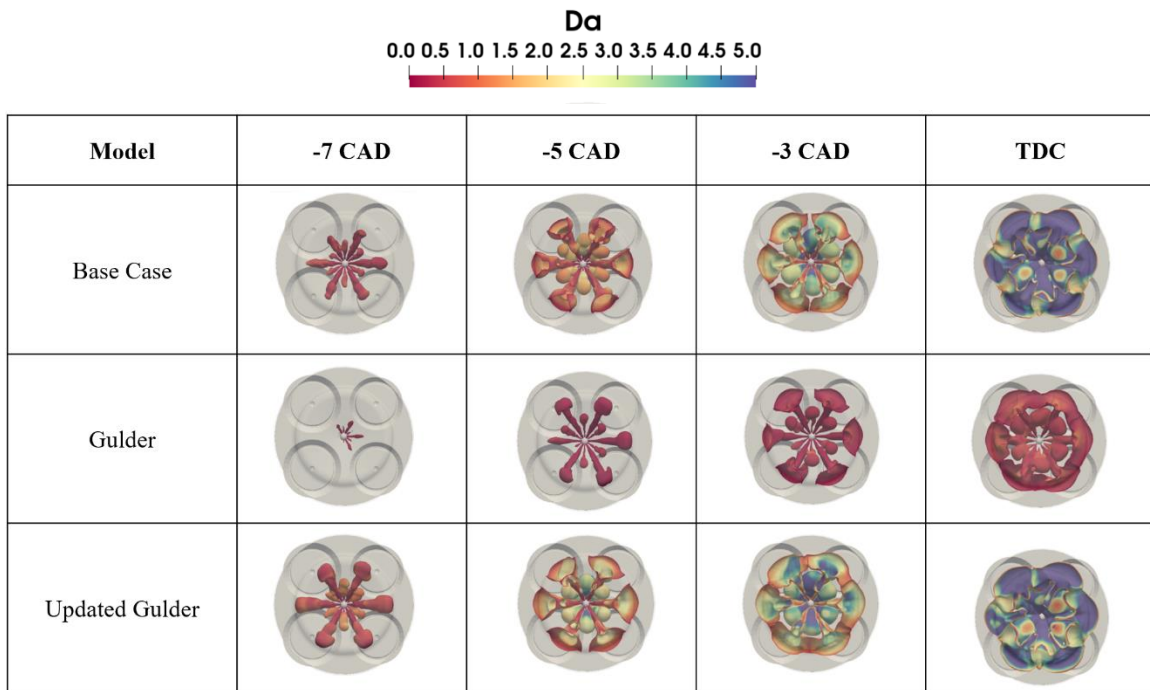


Figure 20: 3D results of flame topology and Damköhler number within the main chamber region for the three models for the case of PCFR 7%

The behavior of the flame front for all three models with PCFR 7% is similar to those in the case of PCFR 3%. The baseline model calculates a  $u'/S_L$  ratio that places the flame front in the thin reaction zone at the start of combustion and eventually moves to the corrugated flamelet regime around TDC. Gulder's original model calculates a smaller laminar flame speed which, consequently, calculates a large  $u'/S_L$  that predicts a flame front in the broken reaction zone. Since the  $G$ -equation is not applicable when the flame front is in the broken reaction zone, the combustion model that uses Gulder's correlation to calculate  $S_L$  is not valid and, hence, fails at predicting pressure build up and the flame topology in both the prechamber and main chamber. The small, yet acceptable, differences

seen in figure 22 are consistent with the faster flame development seen in the 3D results of the optimized model in the pre and main chambers.

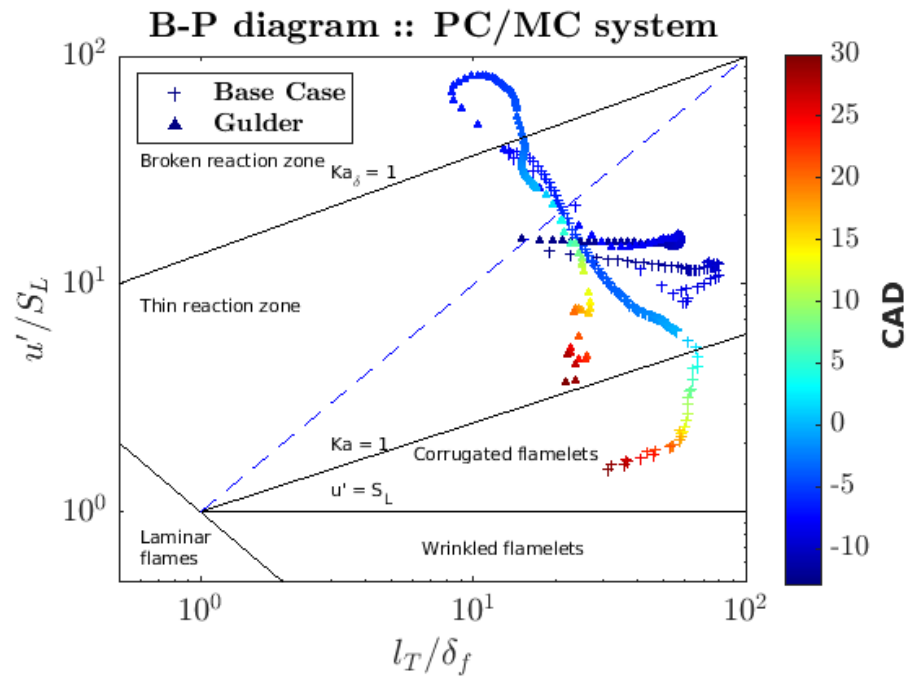


Figure 21: Borghi-Peters diagram for PCFR 7% showing the base case and Gulder's original model

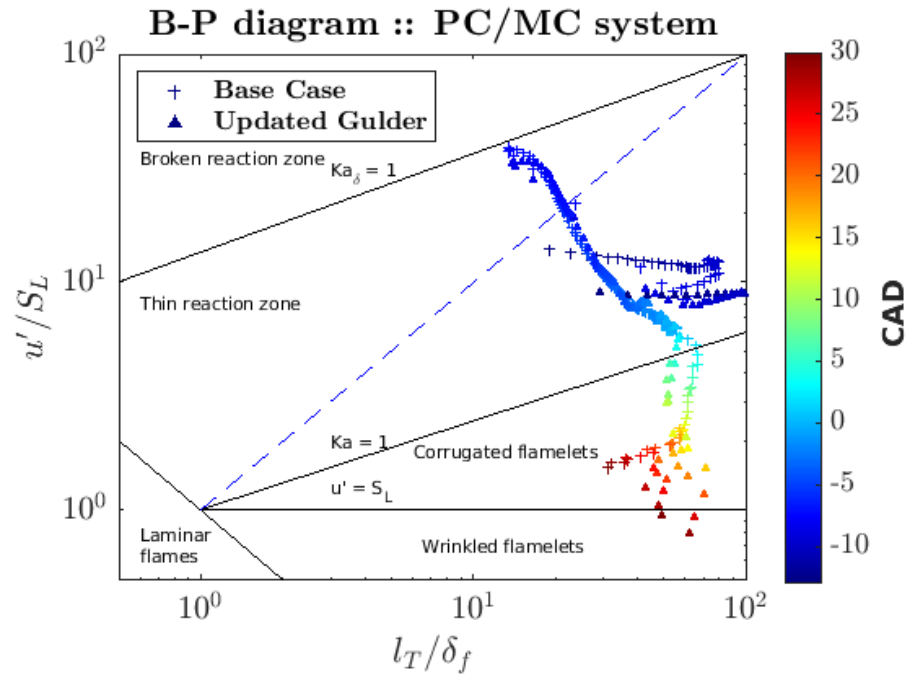


Figure 22: Borghi-Peters diagram for PCFR 7% showing the base case and Gulder's updated model

### 5.2.2 PCFR 13%

The prechamber composition for a PCFR of 13% is extremely rich with an average of  $\lambda = 0.5$ . Unlike the two previous cases, for the case of PCFR 13%, Gulder's original model fails to predict the pressure profile even before TDC as seen in figure 23. Both the maximum prechamber pressure and the profile do not match the average experimental data nor the reference case. It is also observed in figure 23 that while the updated model predicts the average experimental pressure buildup well, the pressure profile of the reference case is slightly delayed compared to the average experimental curve.

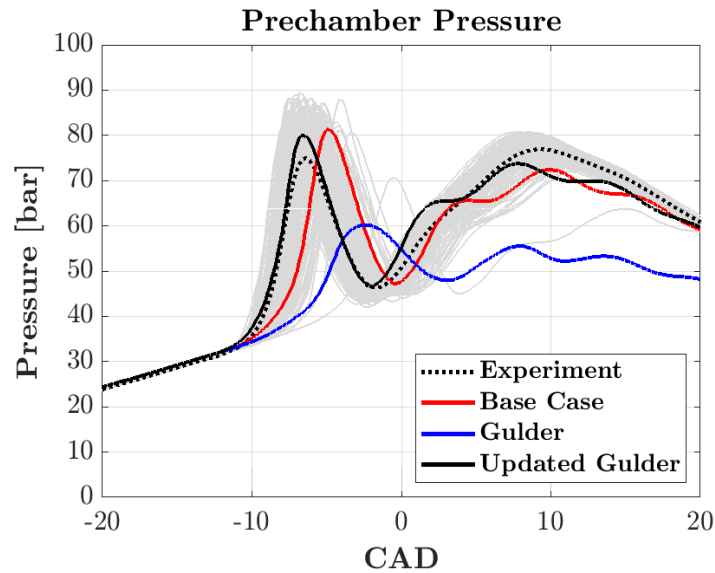


Figure 23: Prechamber pressure as predicted by the reference case, Gulder's original model, and Gulder's updated model for the case of PCFR 13%

For the baseline case, figure 24 shows that the amount of fuel consumed by the time the flame is at the entrance of the throat region is clearly smaller than the fuel consumed in the case of the updated Gulder's model. Since the pressure buildup is a reflection of the fuel consumed, the delay in the pressure increase for the baseline case is a result of the smaller amount of fuel consumed. Further investigation of the chemical mechanism is needed to understand the reason behind the reduced fuel consumption in the case of extremely rich prechamber. The effect of Gulder's slow speed is also observed early in the prechamber. At -8 CAD, the flame development is slower and the fuel consumed is even smaller than the baseline case.



Model	-8 CAD	Before entering the throat region	Da number in the throat region	Before exiting the throat region
Base Case		-6.9 CAD	-6.5 CAD	-6.5 CAD
Gulder		-5.2 CAD	-4.5 CAD	-4.8 CAD
Updated Gulder		-7.7 CAD	-7.2 CAD	-7.3 CAD

Figure 24: 3D results of flame topology and Damköhler number within the prechamber region for the three models for the case of PCFR 13%

Within the main chamber region, the same pattern observed in figure 13 and figure 19 is found in figure 25. Gulder's original model predicts a similar pressure profile as the experimental results and the other two models until TDC. Figure 17 shows that before TDC, the reference model and Gulder's updated model have Damköhler numbers smaller than unity, but they become larger than unity by TDC. The original model, on the other hand, has a much slower flame that does not enter the prechamber until after -5 CAD with Damköhler numbers smaller than unity even at TDC.

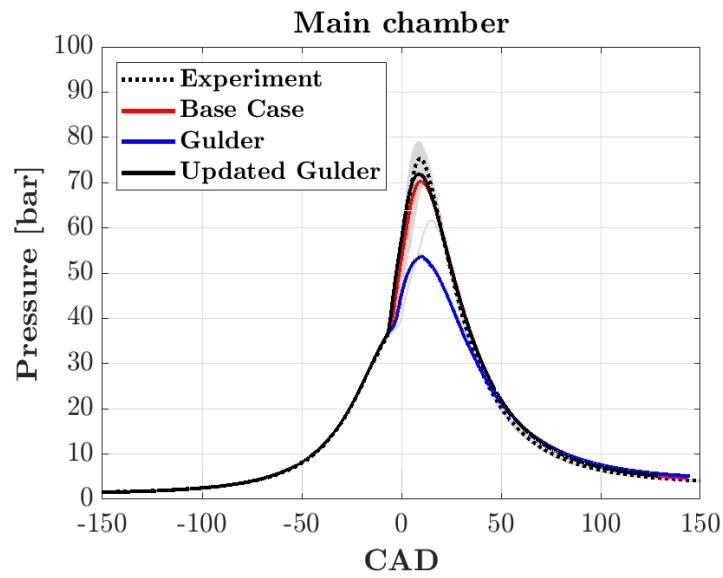


Figure 25: Main chamber pressure as predicted by the reference case, Gulder's original model, and Gulder's updated model for the case of PCFR 13%

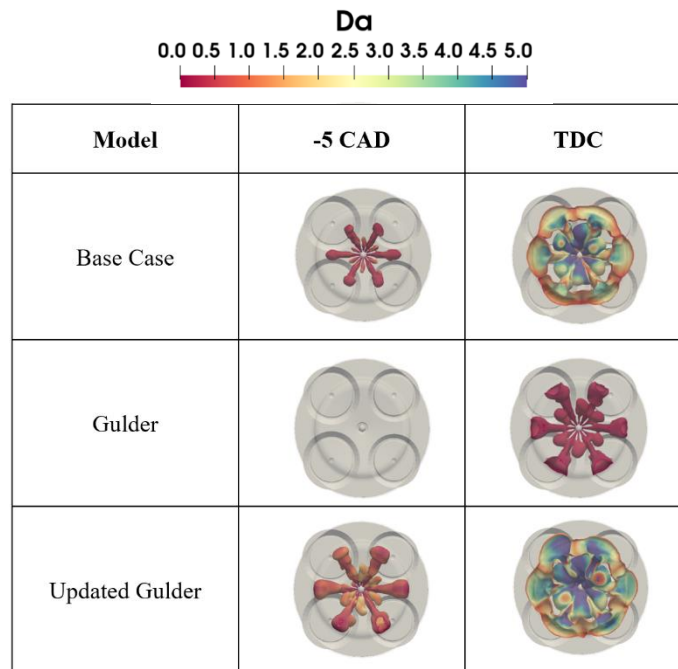


Figure 26: 3D results of flame topology and Damköhler number within the main chamber region for the three models for the case of PCFR 13%

The Borghi-Peters diagram for the reference case and Gulder's model is shown in figure 27. Similar to the previous two cases, Gulder's flame front enters the broken reaction zone, in this case around TDC, due to the slow  $S_L$ . This result can explain the behavior seen in figure 23 and figure 25. Once the flame enters the broken reaction zone, Gulder's pressure prediction fails to match the experimental data and the reference case since the combustion model is no longer valid. On the other hand, the updated model's flame remains within the thin reaction and corrugated flamelet zones. With small expected differences, the updated model shows similar flame front behavior to the baseline case in figure 28.

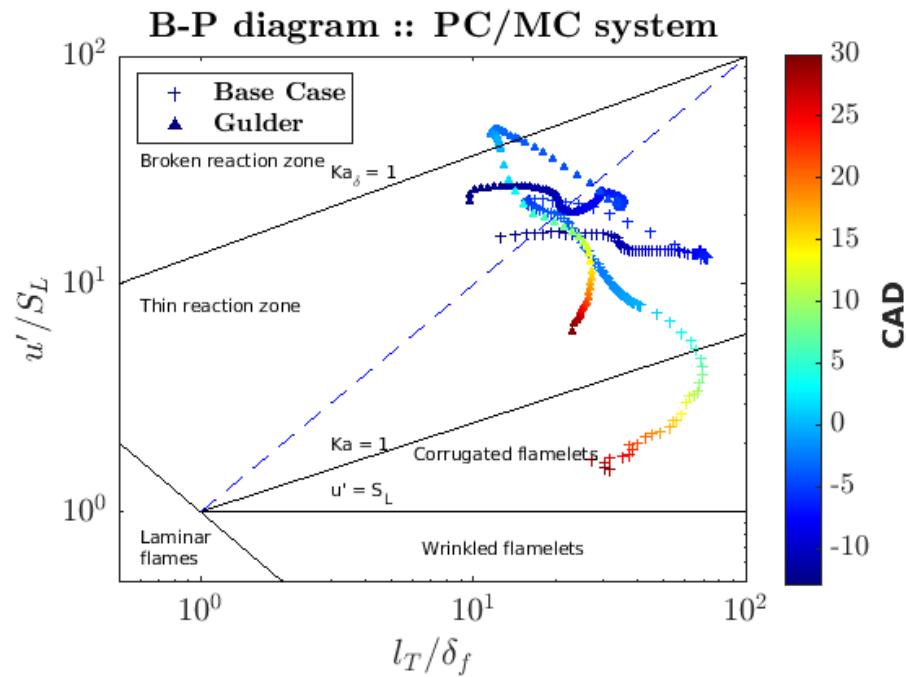


Figure 27: Borghi-Peters diagram for PCFR 13% showing the base case and Gulder's original model

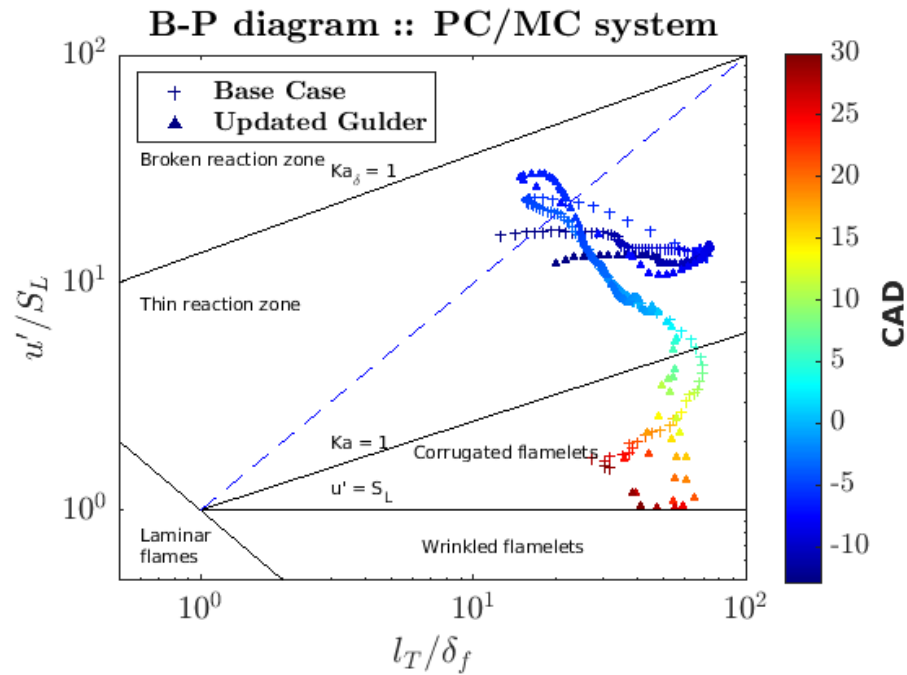


Figure 28: Borghi-Peters diagram for PCFR 13% showing the base case and Gulder's updated model

## 5.4 Summary

The CFD simulations and 3D flame topology are investigated for the three models that have the same formula (Peters' correlation) to calculate the turbulent flame speed but different laminar flame speeds using reference skeletal GRI 3.0, Gulder's original model, and Gulder's updated model, respectively. With a global air-fuel ratio of  $\lambda = 1.8$ , three different prechamber compositions are explored: PCFR 3%, 7%, and 13%. In all three cases, the skeletal GRI 3.0 model is used as a reference since it produces satisfactory pressure predictions in both the prechamber and main chamber as compared to the experimental engine results. Gulder's original model does not show an adequate estimation

of the main chamber pressure in all three PCFR cases, while the prechamber pressure is acceptably predicted in the case of the PCFR 3% and 7% prior to TDC. Gulder's updated model, however, predicts the pressure profiles well and matches the reference case for the three cases. The flame topology and the analysis of the Borghi-Peters diagram further explain the trends found in the CFD simulations.

## Chapter 6

### Conclusion and Future Work

A mismatch is observed between the KAUST experimental results and the CFD simulations conducted in CONVERGE that use the *G*-Equation for the combustion modeling coupled with SAGE chemistry solver and Gulder model's for the calculation of the laminar burning velocity. When using the tabulated  $S_L$  from the skeletal GRI 3.0 chemical mechanism with the *G*-equation, a better match between the simulations and the experimental results is obtained. In previous work [8], the mismatch between the simulations and the experimental results has been blamed on the calculation of the turbulent flame speed by Peters' model. However, the turbulent flame speed was unchanged in both cases where a mismatch was observed and where a perfect match was obtained. It is the laminar flame speed, therefore, that is believed to be the reason that the simulations using Gulder's model underpredict the peak pressure.

Since the empirical constants in Gulder's model for laminar flame speed were selected by Gulder for the prediction of  $S_L$  at ambient and near-ambient temperature and pressure, such constants are altered to fit the defined engine conditions. Many previous works modified the same constants to fit a wider range of composition and a higher range of temperature and pressure [12, 13, 22-24]. However, this work explores the range of composition, temperature, and pressure found in real prechamber engines.

The adjustment of Gulder's constants was made to ensure that the new model predicts similar values of  $S_L$  as those calculated in Chemkin using the skeletal GRI 3.0 chemical mechanism. A thorough investigation was made to confirm that the constants altered are changed within a reasonable and acceptable range and not modified arbitrarily. The new values were selected in a way that provides a global average minimum difference between the  $S_L$  calculated by Gulder and by the referenced chemical mechanism.

The new adjusted model was then implemented in CONVERGE under three different prechamber compositions to test its applicability. The updated model shows a significant improvement compared to Gulder's original model across all the cases tested. The much improved results highlight the significance of the laminar flame speed in modeling turbulent combustion in prechamber engines. Unlike the previously believed claim that the turbulent flame speed is responsible for the inaccuracy of the predictive modeling of turbulent combustion, the results of this work shows that adjusting the laminar flame speed instead resolves the mismatch between the numerical model and experimental data. In addition, the model constants in Peters' correlation for the turbulent flame speed must not be modified arbitrarily without thorough examination of the physical meaning and mathematical derivation of those constants.

There remains a slight, yet acceptable, difference between the average experimental pressure profile and the simulated profile using the updated model. Such a difference is expected since the new values of the empirical constants were optimized for a wide range of temperature, pressure, and composition. In fact, local conditions across the flame surface are dynamically changing and the model constants should do so as well. The work of

Varghese et al [23] provides such a dynamic value for the temperature exponent as a function of the pressure and composition within a limited range of composition and pressure. Future work will target the assessment of the three model constants investigated in this work  $\alpha$ ,  $\eta$ , and  $\xi$ , while updating them dynamically for the range of engine conditions, thus extending the predictive modeling capabilities and accuracy.

Furthermore, future efforts can be dedicated to using machine learning to analyze the KAUST experimental data to optimize Gulder's constants more efficiently and accurately. Using the earlier presented 1-D laminar flame speed calculations, a more optimized set of empirical constants can be calculated. More constants within the correlation could also be investigated to produce a more fitting expression of Gulder's model to the engine conditions discussed in this work.

## BIBLIOGRAPHY

1. Toulson, E., H.J. Schock, and W.S. Attard, *A Review of Pre-Chamber Initiated Jet Ignition Combustion Systems*. SAE Powertrains Fuels & Lubricants Meeting, 2010. **2263**.
2. Xu, G., et al., *Characterization of combustion in a gas engine ignited using a small un-scavenged pre-chamber*. International Journal of Engine Research, 2020. **21**(7): p. 1085-1106.
3. Silva, M., et al., *A Computational Investigation of Fuel Enrichment in the Pre-Chamber on the Ignition of the Main Chamber Charge*, in *SAE Technical Paper Series*. 2021.
4. Shah, A., P. Tunestal, and B. Johansson, *Effect of Pre-Chamber Volume and Nozzle Diameter on Pre-Chamber Ignition in Heavy Duty Natural Gas Engines*, in *SAE Technical Paper Series*. 2015.
5. Silva, M., et al., *Effects of Geometry on Passive Pre-Chamber Combustion Characteristics*, in *SAE Technical Paper Series*. 2020.
6. Thelen, B.C. and E. Toulson, *A computational study on the effect of the orifice size on the performance of a turbulent jet ignition system*. Proceedings of the Institution of Mechanical Engineers, Part D: Journal of Automobile Engineering, 2016. **231**(4): p. 536-554.
7. Sanal, S., et al., *A Numerical Study on the Ignition of Lean CH<sub>4</sub>/Air Mixture by a Pre-Chamber-Initiated Turbulent Jet*, in *SAE Technical Paper Series*. 2020.
8. Kim, J., et al. *Assessment of Turbulent Combustion Models for Simulating Pre-Chamber Ignition in a Natural Gas Engine*. in *ASME 2019 Internal Combustion Engine Division Fall Technical Conference*. 2019.
9. Peters, N., *Turbulent Combustion*. Cambridge Monographs on Mechanics. 2000, Cambridge: Cambridge University Press.
10. Law, C.K., *Combustion Physics*. 2006, Cambridge: Cambridge University Press.
11. Gülder, Ö.L., *Correlations of Laminar Combustion Data for Alternative S.I. Engine Fuels*. 1984, SAE International.
12. Andrews, G.E. and D. Bradley, *The Burning Velocity of Methane-Air Mixtures*. Combustion and Flame, 1972. **19**: p. 275-288.

13. Babkin, V.S. and L.S. Kozachenko, *Study of normal burning velocity in methane-air mixtures at high pressures*. Combustion, Explosion and Shock Waves, 1966. **2**(3): p. 46-52.
14. Vagelopoulos, C.N. and F.N. Egolfopoulos, '*Direct Experimental Determination of Laminar Flame Speeds*'. WSS/CI 97S-022, 1997. **Western States Section/Combustion Institute Meeting, Livermore, CA.**
15. Lu, T. and C.K. Law, *A criterion based on computational singular perturbation for the identification of quasi steady state species: A reduced mechanism for methane oxidation with NO chemistry*. Combustion and Flame, 2008. **154**(4): p. 761-774.
16. Metcalfe, W.K., et al., *A Hierarchical and Comparative Kinetic Modeling Study of C1-C2 Hydrocarbon and Oxygenated Fuels*. International Journal of Chemical Kinetics, 2013. **45**(10): p. 638-675.
17. *Chemical-Kinetic Mechanisms for Combustion Applications*. San Diego Mechanism web page **Mechanical and Aerospace Engineering (Combustion Research)**.
18. Han, Z. and R.D. Reitz, *Turbulence Modeling of Internal Combustion Engines Using RNG  $\kappa$ - $\epsilon$  Models*. Combustion Science and Technology, 1995. **106**(4-6): p. 267-295.
19. Williams, F.A., *Combustion Theory*. 1985.
20. Kee, R.J., et al., *CHEMKIN Collection*. San Diego, CA (2000).( Release 3.6).
21. Silva, M.M., *A Numerical Investigation of Pre-chamber Combustion Engines*. 2020, King Abdullah University of Science and Technology (KAUST).
22. Konnov, A.A., *The Temperature and Pressure Dependences of the Laminar Burning Velocity: Experiments and Modelling*. Proceedings of the European combustion meeting, Budapest, Hungary, 2015.
23. Varghese, R.J., et al., *Measurement of laminar burning velocities of methane-air mixtures simultaneously at elevated pressures and elevated temperatures*. Fuel, 2019. **257**.
24. Han, P., et al., *Burning velocity of methane/diluent mixture with reformer gas addition*. Fuel, 2007. **86**(4): p. 585-596.